

Variable late Neogene exhumation of the central European Alps: Low-temperature thermochronology from the Aar Massif, Switzerland, and the Lepontine Dome, Italy

Antoine Vernon, Peter A. van Der Beek, H. Sinclair, C. Persano, J. Foeken, F.M Stuart

▶ **To cite this version:**

Antoine Vernon, Peter A. van Der Beek, H. Sinclair, C. Persano, J. Foeken, et al.. Variable late Neogene exhumation of the central European Alps: Low-temperature thermochronology from the Aar Massif, Switzerland, and the Lepontine Dome, Italy. Tectonics, 2009, 28, pp.TC5004. 10.1029/2008TC002387 . insu-00411867

HAL Id: insu-00411867
https://insu.hal.science/insu-00411867

Submitted on 4 Mar 2021

HAL is a multi-disciplinary open access archive for the deposit and dissemination of scientific research documents, whether they are published or not. The documents may come from teaching and research institutions in France or abroad, or from public or private research centers.

L'archive ouverte pluridisciplinaire **HAL**, est destinée au dépôt et à la diffusion de documents scientifiques de niveau recherche, publiés ou non, émanant des établissements d'enseignement et de recherche français ou étrangers, des laboratoires publics ou privés.

Variable late Neogene exhumation of the central European Alps: Low-temperature thermochronology from the Aar Massif, Switzerland, and the Lepontine Dome, Italy

Antoine J. Vernon,[1,2,3] Peter A. van der Beek,[1] Hugh D. Sinclair,[2] Cristina Persano,[4] Jurgen Foeken,[5] and Finlay M. Stuart[5]

Received 2 September 2008; revised 5 April 2009; accepted 2 July 2009; published 16 September 2009.

[1] Several recent studies proposed an important increase in exhumation rate in the western European Alps since circa 5–4 Ma. In order to assess potential spatial differences in exhumation histories, we present new apatite fission track (AFT) and apatite (U-Th)/He (AHe) ages from the central Aar Massif (Guttannen area, Switzerland) and the western Lepontine Dome (Formazza area, Italy). Internal U/Th zoning in apatites explains alpha-ejection-corrected AHe ages that are older than the corresponding AFT ages in this study. A qualitative interpretation of AFT and AHe age-elevation relationships suggests a two-phase (9–7 and 5–3 Ma) exhumation scenario affecting the central Alps, with a stronger expression of the Pliocene signal in the Formazza area. However, a quantitative evaluation of exhumation scenarios using the 3-D heat equation solver Pecube highlights the existence of several other likely scenarios, casting doubt on the validity of a qualitative interpretation of the age-elevation relationships. In Formazza, scenarios suggested by quantitative modeling include continuous denudation at a rate of ~750 m/Ma and a one-step exhumation rate change from 300 to 1000 m/Ma at 5 Ma. In Guttannen, they include continuous denudation at a rate of ~400 m/Ma with valley deepening and two periods of higher exhumation rate (increasing from 300 to 700 m/Ma repeatedly at 9–7 and at 5–3 Ma). Contingent upon further flexural isostatic modeling, the magnitude of exhumation recorded in the axial region of the Alps since circa 5 Ma does not appear sufficient to solely explain the denudation recorded in the North Alpine Foreland Basin. **Citation:** Vernon, A. J., P. A. van der Beek, H. D. Sinclair, C. Persano, J. Foeken, and F. M. Stuart (2009), Variable late Neogene exhumation of the central European Alps: Low-temperature thermochronology from the Aar Massif, Switzerland, and the Lepontine Dome, Italy, *Tectonics*, *28*, TC5004, doi:10.1029/2008TC002387.

1. Introduction

[2] Sediment volumes from around the globe record an increase in sediment accumulation rates during the Pliocene [*Davies et al.*, 1977; *Zhang et al.*, 2001; *Molnar*, 2004]. This increase is also recorded by sediments shed from the European Alps [*Kuhlemann*, 2000; *Willett et al.*, 2006]. Together with the documented exhumation of the North Alpine Foreland Basin since circa 5–4 Ma, this observation led *Cederbom et al.* [2004] to propose that the bulk of the Alps experienced accelerated exhumation and isostatic rebound since Early Pliocene times. Evidence for significant tectonic deformation during this period is not compelling, and therefore climate change has been proposed as the driving mechanism for increased erosion rates [*Cederbom et al.*, 2004]. Consequently, the axial Alpine crystalline massifs should have been subjected to accelerated denudation during the Pliocene. The uniquely dense apatite fission track (AFT) record in the western European Alps has been used to derive exhumation rates for the period spanning from 13.5 to 2.5 Ma [*Vernon et al.*, 2008]. In addition to supporting the hypothesis of overall accelerating denudation around 5 Ma, this analysis reveals a spatial diachroneity in exhumation on 50–100 km wavelengths, with accelerations starting between 6.5 Ma and 2.5 Ma or later [*Vernon et al.*, 2008]. Refining the description of this heterogeneity in exhumation history by further and more detailed thermochronometric analyses may be key to distinguish between a model of variable, but diffuse exhumation since 5 Ma, in response to the erosional decay of the orogen, versus a model of localized exhumation associated with differential rock uplift across active faults during the late stages of plate convergence.

[3] Here, we test for regional variations in late Neogene exhumation along a north-south transect in the central Alps (Figures 1 and 2). We use apatite fission track (AFT) and apatite (U-Th)/He (AHe) ages along elevation profiles from the Aar Massif and the Lepontine Dome, completed by fifteen samples along the transect (Table 1). The transect projects into the mountain belt from the well data of the North Alpine Foreland Basin studied by *Cederbom et al.* [2004]. After describing the dating methods and results, we

[1]Laboratoire de Géodynamique des Chaînes Alpines, Université Joseph Fourier, Grenoble, France.
[2]School of Geosciences, University of Edinburgh, Edinburgh, UK.
[3]Now at Department of Geosciences, University of Arizona, Tucson, Arizona, USA.
[4]Department of Geographical and Earth Sciences, University of Glasgow, Glasgow, UK.
[5]Isotope Geosciences Unit, Scottish Universities Environmental Research Centre, East Kilbride, UK.

Copyright 2009 by the American Geophysical Union.
0278-7407/09/2008TC002387

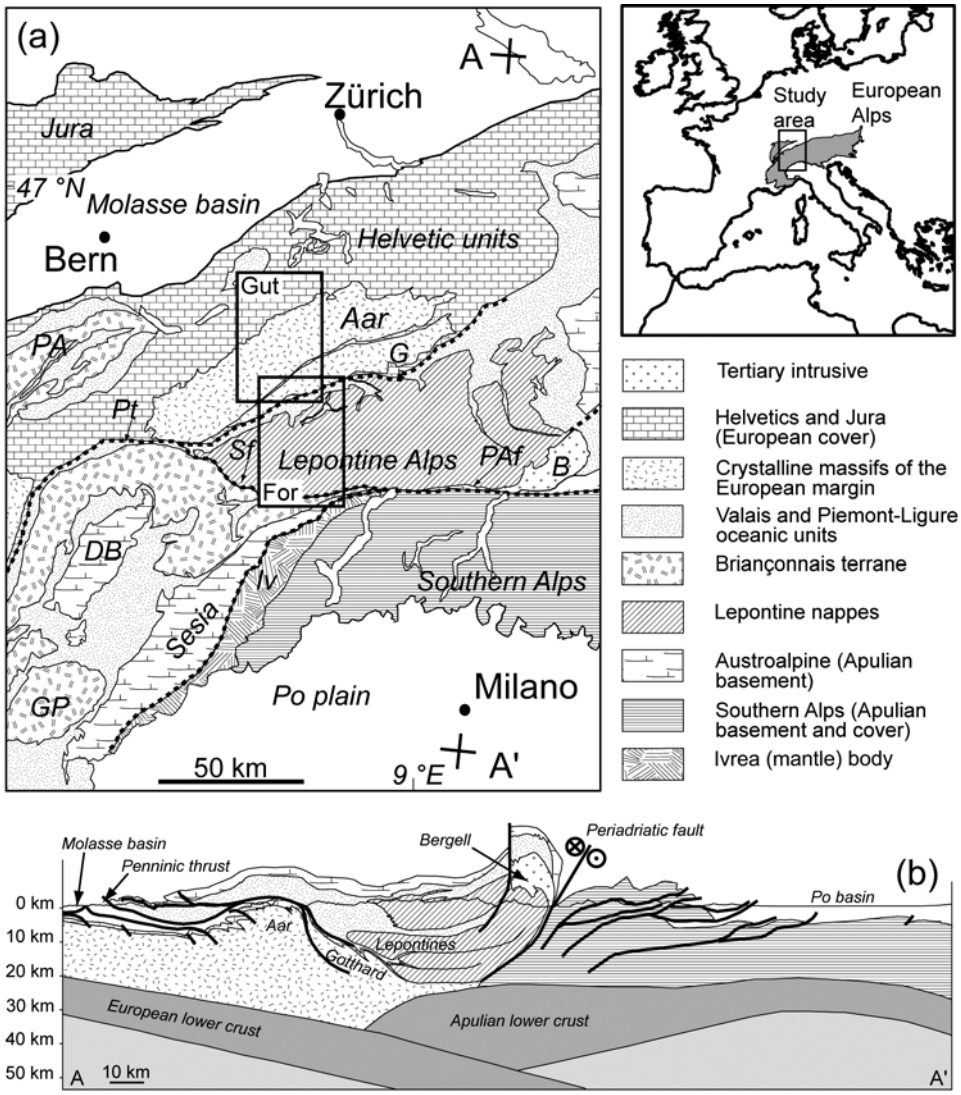


Figure 1. (a) Simplified geological map of the study area [after *Schmid et al.*, 2004]. Abbreviations are B, Bergell; DB, Dent Blanche Massif; G, Gotthard Massif; GP, Gran Paradiso Massif; Iv, Ivrea body; PA, Prealps; PAf, Peri-Adriatic fault; Pt, Penninic thrust; Sf, Simplon fault. Inset boxes noted Gut and For represent the Guttannen (Switzerland) and the Formazza (Italy), respectively, areas used in Pecube models. (b) Crustal-scale geological cross section along the NFP20-East seismic line (A-A′ in Figure 1a), showing the relationship between the main geological units [after *Schmid et al.*, 1996].

consider the effect of apatite U and Th zonation on alpha-ejection-corrected AHe ages and propose that such zonation may constitute an explanation for samples where corrected AHe ages are older than AFT ages. We test several exhumation scenarios with a numerical model (Pecube) allowing us to explore the effects of temporally varying exhumation rates and evolving topography on thermochronometric age distributions [*Braun*, 2003]. As a result, we are able to delineate the most likely exhumation histories in the Aar Massif and Lepontine Dome and compare them with a qualitative interpretation of the AFT and AHe data from the elevation profiles. Finally, the best fit exhumation histories are compared to those required by the erosion history of the foreland basin, assuming a simple model of flexural isostatic rebound in response to accelerated erosional unloading of the axial zones [*Cederbom et al.*, 2004].

2. Geological Setting

[4] Our two study areas (Figure 1) are located in the central Aar Massif (Switzerland) and the western part of the Lepontine Dome (Italy, Switzerland). This region is commonly described as belonging to the Western Alps, as defined by the boundary of the Austroalpine Silvretta unit located to the east of the Lepontine Dome [*Kuhlemann*, 2000]. It is bordered to the north by the Préalpes klippen,

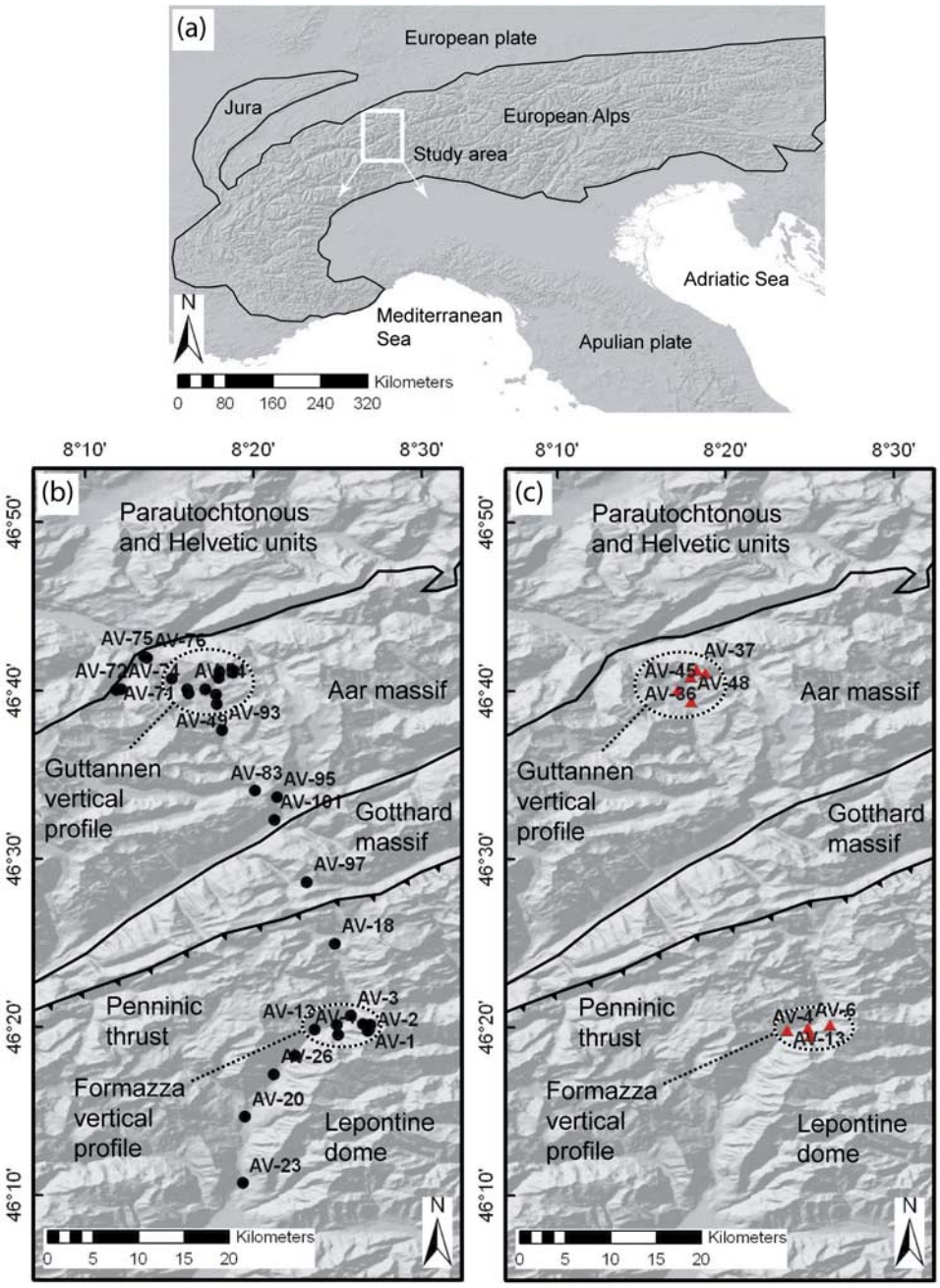


Figure 2. (a) Location map. Maps of (b) AFT and (c) AHe sampling, overlain on shaded relief model of study area (see Figure 2a for location). Main tectonic units and structures are also indicated.

Helvetic units, and perialpine sediments of the North Alpine Foreland Basin [*Homewood et al.*, 1986]. To the south, it is bordered by the Periadriatic line, the southern Alps units and the Po plain [*Schmid et al.*, 2004; *Fantoni et al.*, 2004]. Whereas the North Alpine Foreland Basin has been exhuming since circa 5–4 Ma [*Cederbom et al.*, 2004], the Po Basin accumulated post-Messinian sediments lying unconformably over the southernmost South Alpine thrusts [*Fantoni et al.*, 2004; *Scardia et al.*, 2006].

[5] The Aar-Gotthard Massif is one of the external crystalline massifs that expose the precollision European margin basement. They comprise pre-Variscan and Variscan metasediments, anatectic migmatites, metasedimentary and granitic gneisses, and volcanoclastic sediments [*Abrecht*, 1994; *von Raumer et al.*, 1999] that strike approximately parallel to the Alps. The massifs have experienced Variscan amphibolite facies metamorphism followed by retrograde metamorphism to greenschist facies [*Abrecht*, 1994]. Alpine strain is

Table 1. Sample Details[a]

Sample	Latitude	Longitude	Elevation (m)	Location	Lithology
			Guttannen Area		
AV29	8.314113	46.68528	2800	Furtwangstock	K-feldspar orthogneiss
AV28	8.313765	46.68393	2720	Furtwangstock	Orthogneiss
AV37	8.305003	46.68782	2460	Wannis lake	Orthogneiss
AV35	8.300052	46.68471	2200	Wannis lake	Orthogneiss
AV36	8.29868	46.68068	2103	Wannis lake	Orthogneiss
AV39	8.299301	46.67865	2000	Wannis lake	Orthogneiss
AV45	8.286386	46.66772	1505	Wysstanni	Orthogneiss
AV47	8.296753	46.66225	1303	Wysstanni	Micaschist
AV48	8.29927	46.65616	1210	Guttannen, Vorses	Biotite orthogneiss
AV49	8.297264	46.65325	1095	Furen	Quartzite, with epidote
AV50	8.269657	46.66335	1000	Boden	Orthogneiss
AV54	8.26842	46.66786	900	Boden	Porphyroid orthogneiss
AV70	8.253222	46.67831	780	Boden	Muscovite granitoid
			Formazza Area		
AV1	8.447009	46.32905	2400	Fondovalle	Biotite and garnet micaschist
AV10	8.448012	46.33062	2280	Fondovalle	Paragneiss
AV2	8.449394	46.3351	1993	Fondovalle	Micaschist
AV11	8.441943	46.33607	1740	Fondovalle	Porphyroid orthogneiss
AV12	8.437074	46.33611	1625	Fondovalle, Rido	Orthogneiss
AV4	8.4174	46.32549	1365	Foppiano, Alpe Croce	Deformed granitoid
AV3	8.430079	46.34427	1240	Fondovalle dorf	Deformed granitoid
AV6	8.415249	46.33226	1095	Foppiano	Paragneiss
AV14	8.416279	46.33539	1020	Alpe Cneila, new tunnel	Deformed granitoid
AV13	8.394115	46.33064	895	Chioso	Orthogneiss
			N-S Transect		
AV75	8.225759	46.69964	640	Innertkirchen	Deformed granitoid
AV76	8.228674	46.69782	770	Bim Chapel	Biotite orthogneiss
AV72	8.200137	46.66766	1005	Urbach Tal	Granitoid
AV74	8.203077	46.66764	905	Urbach Tal	Micaschist
AV71	8.198168	46.667	1110	Urbach Tal	Orthogneiss
AV93	8.302725	46.62712	1240	Grimsel, Schwarzbrunnenbrig	Orthogneiss
AV83	8.335357	46.56727	2005	Grimselpass	Porphyroid orthogneiss
AV95	8.357095	46.5608	1790	Gletsch	Porphyroid orthogneiss
AV101	8.354433	46.53833	1405	Oberwald, St Niklaus	Orthogneiss
AV97	8.386597	46.47666	2485	Nufenenpass	Biotite orthogneiss
AV18	8.41447	46.41548	1720	La Frua, Alpe Stafel	Micaschist
AV16	8.375162	46.30471	805	San Rocco	Orthogneiss
AV26	8.354082	46.28621	760	Cadarese	Porphyroid orthogneiss
AV20	8.325497	46.24416	520	Verampio	Granitoid
AV23	8.323134	46.1785	370	Ponte Maglio	Orthogneiss

[a]Samples ranked by decreasing elevation or from north to south. Geographical coordinates are given in datum WGS-1984.

recorded in the Aar-Gotthard Massif by the development of ductile shear fabrics, composed of broadly vertical and N60°E bearing foliations and associated shear zones delimiting lenses of less deformed material [*Choukroune and Gapais*, 1983; *Marquer and Gapais*, 1985; *Marquer and Burkhard*, 1992].

[6] The Lepontine Dome records extensive Tertiary amphibolite facies metamorphism, delimited in the south by the Periadriatic line. To the north, metamorphic grade reduces gradually over the Penninic front, and reaches greenschist facies in the Gotthard and Aar massifs [*Frey and Ferreiro Mählmann*, 1999]. The Lepontine Dome is bound to the west and east by two outward dipping normal faults, the Simplon and Forcola faults, respectively. The structure of the Lepontine area is that of a pile of nappes of gneissic and metasedimentary composition pre-Triassic and Mesozoic in age, respectively [*Frey and Ferreiro Mählmann*, 1999]. The peak of metamorphism post-dates nappe emplacement, as isograds crosscut structural boundaries [*Frey and Ferreiro Mählmann*, 1999].

3. Thermochronology

3.1. Sample Collection and Preparation

[7] The Aar-Gotthard Massif and the Lepontine Dome are the sites of many of the early apatite fission track studies in the Alps, which yielded ages ranging from mid-Miocene to Pliocene [e.g., *Wagner and Reimer*, 1972; *Schaer et al.*, 1975; *Hurford*, 1986; *Michalski and Soom*, 1990].

[8] Early AFT studies that estimated exhumation rates by plotting sample elevation against age commonly used transects that either followed the valleys, or that were widely dispersed. In such configurations, the slope of the age-elevation relationship (AER) may be severely overestimated, vertical or even negative, as a consequence of the fact that closure temperature isotherms are not horizontal planes

[*Stüwe et al.*, 1994; *Mancktelow and Grasemann*, 1997; *Braun*, 2002]. In this study, rock samples were collected along two elevation profiles perpendicular to the main valley in the Aar Massif (Guttannen locality, upper Aar valley, Switzerland) and the Lepontine Alps (Formazza locality, Toce valley, Italy), spanning 1800 and 1400 m, respectively, of vertical relief (Figure 2 and Table 1). These two elevation profiles were completed by a north-south profile joining the two localities. Careful assessment of landforms and regional foliations at the sampled outcrops ensured that samples were from in-place bedrock and not from large deep-seated landslides. A standard mineral preparation procedure was applied; following grinding, apatites were extracted from the 80–250 μm fraction by heavy liquid and magnetic techniques.

3.2. Apatite Fission Track Dating

[9] AFT dating was performed using the external detector method [*Gleadow*, 1981]. For each sample, 120 apatite crystals were handpicked under binocular lenses and molded in araldite resin, before being polished and chemically etched for 20 s in a 5.5 M HNO_3 solution at 20°C. A sheet of natural low-U mica used as the induced-track detector was tightly applied against the polished surface before irradiation at the well-thermalized ORPHEE reactor in Saclay (France). NBS962 dosimeter glasses with [U] = 12.3 ppm were included in the irradiation batch in order to calculate the neutron fluence. Several mineral standards (Durango and Fish Canyon apatites) were also included in order to calculate a zeta value [*Hurford and Green*, 1983]. Mica detectors were etched for 20 min in a 40% HF solution at room temperature. A total of 14 zeta measurements on Durango, Fish Canyon and Mont Dromedary apatite standards from several irradiations were used to calculate a weighted average zeta value of 325 ± 25. We counted spontaneous and induced tracks using a Zeiss Axioplan Fission track microscope, under 1250× magnification, with the help of reflected light to distinguish between tracks and crystal dislocations or inclusions. Provided a sufficient number of good quality apatites were present, we counted circa 20 crystals per sample, some of them without spontaneous tracks.

3.3. Apatite (U-Th)/He (AHe) Dating

[10] AHe dating was performed following the method described by *Foeken et al.* [2006] on replicates of single apatite grains carefully picked in clove oil to avoid mineral or fluid inclusion-bearing grains. The length and width of each crystal was measured under a binocular microscope under a magnification of 258× before packing in Pt foil tubes. The He content of single grains was extracted by heating at circa 800°C using a 25 W, 808 nm diode laser, for 2 min, purified in an ultrahigh vacuum line and measured with an electron multiplier in a Hiden HAL3F quadrupole mass spectrometer operated in static mode. Absolute He concentrations were calculated from peak height comparison against a known volume of ^{4}He. The low He content of most samples required a blank correction which represented between 0.4 and 91% of the amount of He measured (grains with blank correction higher than 40% were later discarded; see Table 3). The same laser degassing process was repeated two or three times until reaching blank level He, unless a continuously high amount of gas extracted suggested the presence of an unnoticed inclusion.

[11] U and Th were measured by isotopic dilution with inductively coupled–plasma mass spectrometry (ICP-MS). An average of 0.15 ± 0.009 ng of ^{230}Th and 0.06 ± 0.003 ng of ^{235}U were added as spike to the dissolving 5 M HNO_3 solution and left overnight at 100°C. ICP-MS mass fractionation was accounted for by repeated measurement of a U-500 standard. Blank measurements of nitric acid and spike were used to correct the measured isotopic ratios. The total amounts of U and Th were determined using the formula of *Evans et al.* [2005] and final AHe ages were obtained using the noniterative formula proposed by *Meesters and Dunai* [2005]. Durango apatites (n = 4) yielded an average age of 32.6 ± 0.7 Ma; within the age range (31.1 to 33.4 Ma) accepted by *Boyce and Hodges* [2005].

4. Results

4.1. AFT Ages

[12] AFT central ages were calculated using the Trackkey 4.2g code [*Dunkl*, 2002]; the complementary use of the Binomfit peak age analysis code [*Brandon*, 1992, 1996] enabled detection of outlier grains, which may have an important effect on central age calculations and were thus discarded. Results are reported in Table 2 and Figure 3. In four samples, binomial peak fitting recorded two individual grain age populations representing at least 30% of the number of apatites counted (samples AV01, −54, −70, −75). Among these samples, one is located at the top of the Formazza profile (AV01 in Table 2) and two others at the base of the Guttannen profile (AV54, −70 in Table 2). The last sample showing this behavior, AV75, is located at a lower elevation than the Guttannen profile sensu stricto, further down the valley. All samples are from basement rocks having undergone alpine metamorphism in greenschist or higher facies, which affected most parts of the Aar and Lepontine massifs [*Hunziker et al.*, 1992; *Challandes*, 2001]. Although these conditions must have reset all low-temperature thermochronometers, a range of apatite composition in metasediments affects the closure temperature of each grain [e.g., *O'Sullivan and Parrish*, 1995], thus leading to several groups of single-grain ages within a sample. This effect is stronger in the case of an extended stay in the temperature range corresponding to the AFT partial annealing zone. Unfortunately, the overall low numbers of spontaneous tracks in the analyzed apatites rendered the quantification of track length distributions and subsequent modeling of the cooling histories impossible.

[13] AFT ages for samples from the Guttannen and Formazza elevation profiles are plotted in Figure 4, discarding samples with two major grain age populations. The ages used are either the central age, or the main peak age (P1 age in Table 2) in case of the presence of a few outlier grains. Uncertainty-weighted regression lines and 95% confidence intervals are added to the diagrams, along with the slope of

Table 2. AFT Dating Results[a]

Sample	N	ρ_s	N_s	ρ_i	N_i	ρ_d	N_d	P (χ^2)	D	Age	Age 1σ	P1 Age	P1 Age 1σ	P1%	P2 Age	P2 Age 1σ	P2%	[U]	Δ[U]
Guttannen Section																			
AV29	22	3.24	463	31.93	4558	5.302	9317	68.6	0	8.7	0.8	8.7	0.8	100				74	29
AV28	22	1.35	246	13.89	2534	5.492	7546	58.2	6	8.7	0.9	8.7	0.9	100				33	61
AV35	22	4.79	919	49.49	9490	5.491	7546	0.2	16	8.7	0.8	8.3	0.8	93.2	14.6	4.1	6.8	112	31
AV39	22	5.03	937	51.89	9666	5.491	7546	17.3	7	8.6	0.7	8.4	0.8	93.3	12.9	3.1	0.7	116	18
AV45	21	4.44	586	54.97	7252	5.240	7463	72.1	0	6.9	0.6	6.9	0.6	100				129	22
AV47	22	3.97	438	52.60	5797	5.490	7546	65.9	0	6.7	0.6	6.7	0.7	100				118	23
AV49	7	1.2	63	13.1	679	5.490	7546	81.4	0	8.3	1.3	8.3	1.3	100				29	27
AV50	22	3.90	511	49.66	6515	5.810	9647	51.6	8	7.4	0.7	7.7	0.8	93.3	4.7	1.25	6.7	103	28
AV54[b]	21	2.78	320	41.44	4776	5.489	7546	3.7	18	6.1	0.6	7.1	1.2	61	4.7	1	39	91	25
AV70[b]	19	4.38	465	54.56	5797	5.489	7546	4.6	16	7.3	0.7	8.2	1.0	70	5.4	0.85	30	123	42
Formazza Section																			
AV1[b]	23	0.48	68	6.75	959	5.310	9317	19.3	30	6.2	1	7.7	2.2	69.4	3.2	2.1	30.6	16	31
AV10	22	0.45	66	9.075	1338	5.495	7546	16.3	28	4.5	0.7	3.6	0.9	80.5	8.4	4.3	19.5	21	56
AV2	21	0.43	60	8.332	1175	5.496	7546	53.0	3	4.6	0.7	4.6	0.7	100				18	38
AV11	16	0.42	32	11.2	855	5.813	9647	65.1	11	3.5	0.7	3.5	0.7	100				23	63
AV4	21	0.37	55	6.62	976	5.496	7546	0.2	50	5.1	1	4.7	0.8	95.5	46.9	40.95	4.5	14	65
AV3	20	0.34	42	8.020	1004	5.496	7546	65.7	2	3.7	0.7	3.7	0.7	100				17	41
AV14	20	0.38	34	8.01	715	5.812	9647	66.2	3	4.5	0.9	4.5	0.9	100				17	42
AV13	21	0.41	59	7.632	1091	5.495	7546	76.1	0	4.8	0.7	4.8	0.8	100				18	46
N-S Transect																			
AV75[b]	20	1.85	316	22.66	3876	5.810	9647	13.3	15	7.7	0.8	6.8	1.1	67.1	9.6	2.25	32.9	48	21
AV76	20	5.29	655	57.58	7128	5.270	7463	0.1	9	7.9	0.8	7.6	0.7	80.1	11.9	1.75	14.7	133	36
AV72	6	2.3	59	31.8	814	5.286	7463	30.9	6	6.2	1	6.2	1.0	100				71	36
AV74	21	2.16	322	30.70	4572	5.810	9647	57.4	2	6.6	0.6	6.6	0.7	100				65	25
AV71	19	3.63	368	44.82	4542	5.278	9317	45.6	4	6.9	0.7	6.8	0.7	94	10.3	4.7	6	113	43
AV93	6	0.44	12	5.25	142	5.317	7463	52.3	0	7.3	2.3	7.3	2.3	100				12	38
AV83	10	0.66	33	7.14	359	5.301	7463	95.8	0	7.9	1.6	7.9	1.6	100				20	70
AV95	17	1.12	102	14.85	1349	5.811	9647	72.4	2	7.1	0.9	7.1	0.95	100				31	47
AV101	15	2.8	88	55.48	1769	5.378	7463	0.3	49	4.6	0.9	3.6	1.0	86	11	4.05	14	112	59
AV97	25	0.41	77	5.867	1093	5.332	7463	6.7	6	6.1	0.9	6	1.0	97.9	20.7	58	2.1	13	48
AV18	20	0.44	58	6.16	807	5.494	7546	58.8	0	6.4	1	6.4	1.0	100				13	64
AV16	17	0.49	62	12.86	1623	5.494	7546	94.2	0	3.4	0.5	3.4	0.6	100				28	50
AV26	23	0.19	29	6.785	1049	5.492	7546	7.0	37	2.5	0.5	3.1	1	79.9	0.3	9.2	20.1	15	54
AV20	21	0.12	21	2.62	446	5.493	7546	45.0	51	4.1	1.1	3	1.1	85.8	10.2	6.55	14.2	6	72
AV23	25	0.24	57	5.435	1320	5.492	7546	81.0	2	3.9	0.6	3.9	3.9	100				12	34

[a]N, number of apatite grains counted; ρ_s, density of spontaneous tracks (10^5/cm^2); N_s, number of spontaneous tracks; ρ_i, density of induced tracks (10^5/cm^2); N_i, number of induced tracks; ρ_d, density of tracks on irradiation fluence dosimeters (10^5/cm^2); N_d, number of tracks counted on irradiation fluence dosimeters; P(χ^2), probability that the single-grain ages represent one population (%); D, age dispersion (%); Age, central age (Ma); 1σ, uncertainty on central age (Ma); P1 age, major age component in grains age peak analysis (Ma); P1%, percentage of total number of grains in main age peak; P2 age, minor age component in grains age peak analysis (Ma); P2%, percentage of total number of grains in minor age peak; [U], uranium concentration (ppm); Δ[U], uncertainty on uranium concentration (%). Samples are ranked in decreasing elevation order within the Guttannen and Formazza sections and from north to south in N-S transect.

[b]Sample with multiple age populations.

the regression line, which corresponds to the apparent exhumation rate. We performed the age-elevation regression following the method of *Williamson* [1968], with none of the parameters considered as independent. The errors used for AFT ages are the 1σ uncertainty on the central age or main peak age.

[14] Central ages in the Guttannen elevation profile show a positive correlation with elevation (Figure 4), with ages varying from 6.7 ± 0.6 Ma at 1303 m (AV47) to 8.7 ± 0.8 Ma at 2800 m elevation (AV29). The regression relationship is very steep, with an apparent exhumation rate of 1028 ± 459 m/Ma, based on an uncertainty-weighted regression calculation with $r^2 = 0.43$.

[15] Central ages in the Formazza elevation profile are inversely correlated with elevation (Figure 4) and vary between 3.5 ± 0.7 (AV11) and 5.1 ± 1.0 (AV4) Ma, i.e., significantly younger than in the Guttannen profile. The relatively poorly constrained AER of −1966 ± 2309 m/Ma does not rule out a positive apparent exhumation rate of >1200 m/Ma at the 95% confidence level. Negative AERs can also occur when local tilting of the profile has occurred since closure [*Rahn and Grasemann*, 1999], or in large valleys when the topographic slope is modified by relief reduction and becomes less steep than the AFT closure surface [*Braun*, 2002].

[16] A profile of AFT central ages along a N-S transect (Figure 3) illustrates a pattern of older ages over the Aar Massif (Guttannen elevation profile) than over the Lepontine Alps (Formazza profile), with ages around 8–7 Ma and 5–4 Ma, respectively. The ages on the horizontal transect are in agreement with existing data from *Keller et al.* [2005] in the western Lepontine Alps or *Schaer et al.* [1975] and

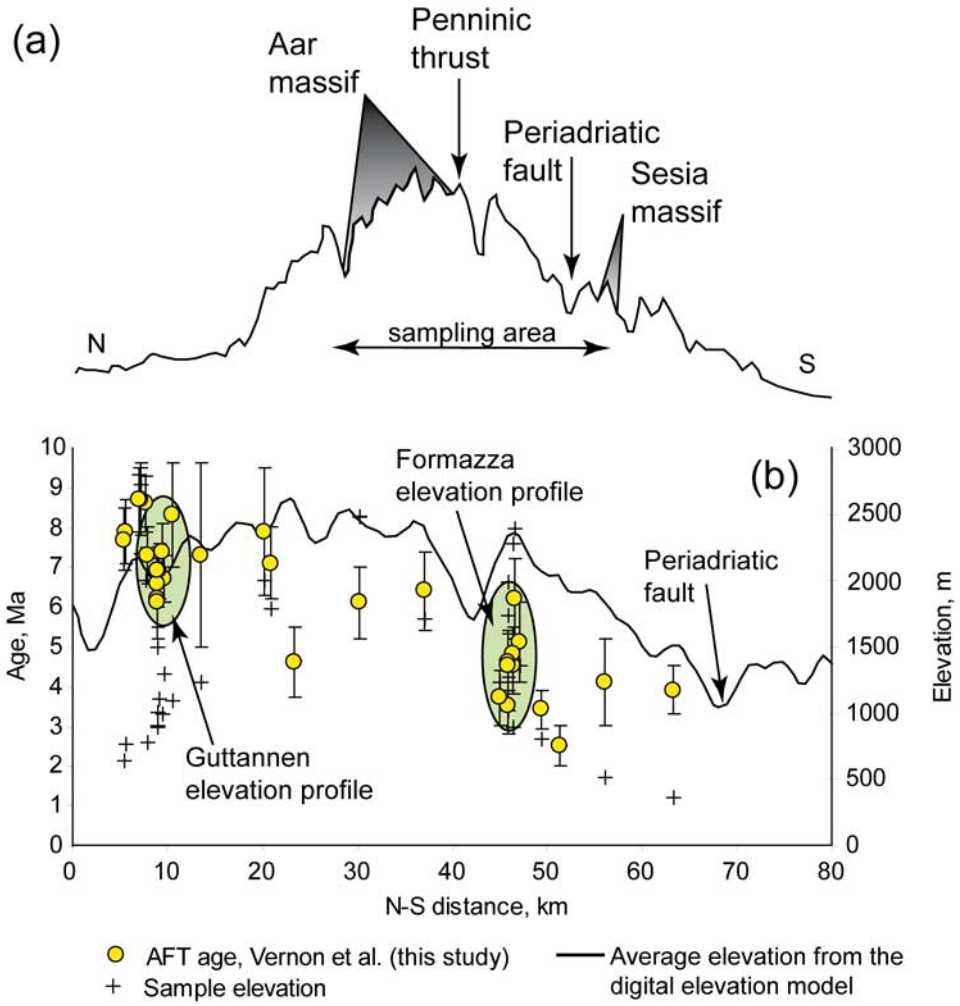


Figure 3. (a) Longitudinal profile of AFT ages. Projection of central AFT ages (circles) obtained in this study on a north-south average topographic cross section joining the Guttannen elevation profile (Switzerland) to the Formazza elevation profile (Italy). (b) A close-up on the sampling area indicated on Figure 3a. Vertical error bars show the 1σ uncertainty on central ages, and crosses show the sample elevation (see Tables 1 and 2). AFT central ages are significantly younger for the Formazza elevation profile than for the Guttannen profile.

Rahn and Grasemann [1999] in the northeastern Aar-Gotthard Massif. AFT ages published by *Michalski and Soom* [1990] for the upper Aar valley upstream and downstream of our elevation profile (12.0 ± 0.9 Ma at 720 m, 4.2 ± 1.1 Ma at 1586 m and 5.3 ± 1.1 Ma at 2160 m) differ from our measurements; however part of the difference may be explained by the relatively low number of spontaneous tracks counted in both studies, and by the lack of good quality apatites.

4.2. AHe Ages

[17] The results for three to five single-crystal replicates for each sample are reported in Table 3. However, we discarded results of several replicates, for reasons detailed in the legend of Table 3, prior to the calculation of uncertainty-weighted average ages (Figure 5).

[18] The age-elevation relationships of uncorrected AHe ages in the Guttannen and the Formazza elevation profiles are presented in Figure 6, using the same method of regression line calculation as described in section 4.1. The justification for using uncorrected ages is outlined in detail in sections 4.3 and 4.4. The Guttannen profile displays a strongly correlated relationship with elevation (r^2 = 0.88) with weighted-mean ages ranging from 5.2 ± 0.5 Ma at 1505 m elevation (AV45) to 9.0 ± 1.3 Ma at 2720 m (AV28), and an apparent exhumation rate of 486 ± 135 m/Ma. In Formazza, the age-elevation relationship is steeper (apparent exhumation rate of 675 ± 539 m/Ma) but less well constrained (r^2 = 0.5). Weighted average AHe ages are also younger, ranging from 2.6 ± 0.2 Ma at 895 m elevation (AV13) to 5.2 ± 2.5 Ma at 1625 m (AV12).

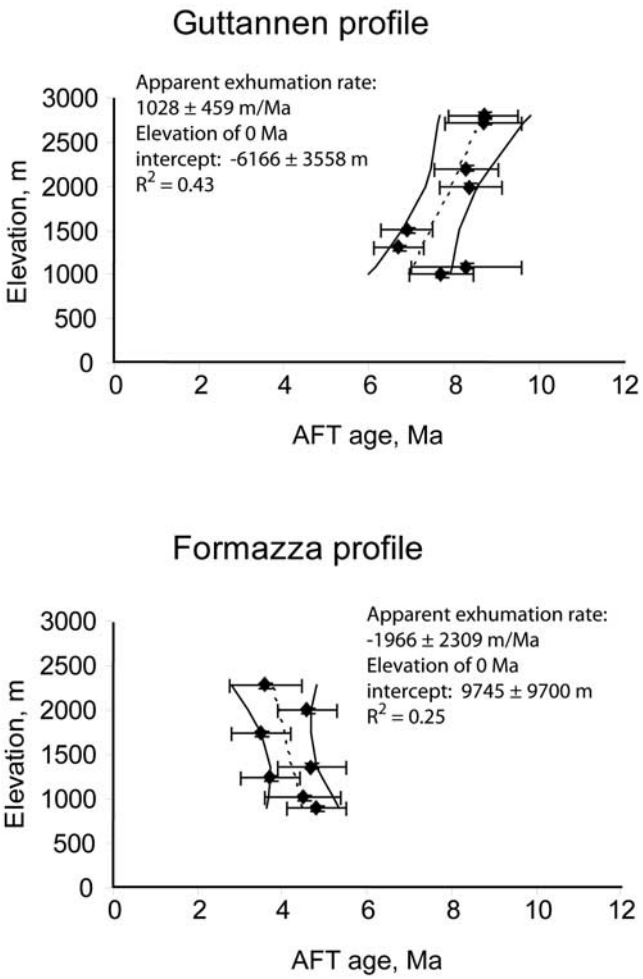


Figure 4. AFT age-elevation profiles and weighted regression relationship (dashed line, regression line; bold lines, 95% confidence interval) for the Guttannen and the Formazza areas. Central ages or main age peak of the AFT age population are plotted with 1σ error bars, excluding samples with a second age peak population comprising more than 30% of the grains counted (AV1, AV54, and AV70).

4.3. Alpha Ejection Correction

[19] In samples with homogeneous U and Th distributions, a significant amount of He is lost by radioactive decay of atoms situated close to the crystal border. The proportion of He loss out of the crystal during the emission of alpha particles decreases from 50% on the grain surface to zero when the emission point is located more than 20 μm from the surface [*Farley et al.*, 1996; *Farley*, 2002]. A correction factor (F_t) based on crystal shape and Th/U ratio therefore needs to be applied to unzoned grains, following the method of *Farley* [2002], in order to make up for the lost He and avoid age underestimation. However, the determination of the grain surface/volume ratio is imprecise and the error on the correction factor Ft is particularly important for small grains [*Farley et al.*, 1996].

[20] The distinctive closure temperatures usually considered for the AFT and AHe thermochronometers (120–90°C and 80–55°C, respectively [*Reiners et al.*, 2005]), lead us to expect AFT ages to be older than AHe ages at a given location. However, several of our corrected AHe ages overlap with, or are older than the AFT ages of the same samples (e.g., AV28 and AV45), or of samples located at similar elevations on an elevation profile (see Figure 7).

4.4. Modeling the Role of Apatite Zoning on AHe Age

[21] Various factors, such as the underestimation of fission track annealing [e.g., *Hendriks and Redfield*, 2005], or the overestimation of He diffusion [*Green et al.*, 2006; *Shuster et al.*, 2006] in radiation-damaged apatite may explain overlap between AHe and AFT ages, particularly in U-rich or old samples. Neither condition, however, is met by our samples. An alternative explanation could be overcorrection of AHe ages by the alpha ejection parameter due to U and Th zonation [*Meesters and Dunai*, 2002b; *Boyce and Hodges*, 2005; *Hourigan et al.*, 2005; *Herman et al.*, 2007]. The correction is underestimated if U and Th are concentrated in the outer 20 μm (external zoning), and overestimated if the outer 20 μm is depleted (internal zoning). Additionally, the F_t correction assumes that the minerals surrounding the apatite grain are devoid of U and Th, whereas in natural rocks several minerals, such as micas, have U and Th concentrations equal to or larger than apatite, which may lead to He implantation in the outer 20 μm of the grain [*Spencer et al.*, 2004].

[22] Strong zoning in induced-track density was observed in apatite grains for several AFT samples (Figure 8). For instance, samples AV2, AV4 or AV13 strikingly displayed prints of induced tracks smaller than the crystal size, suggesting internal zoning. In these conditions, the real AHe age of a crystal would lie between the raw and the corrected values. We assess the effect of U zoning using a Monte Carlo model of He loss out of a crystal or realistic shape with an arbitrary U/Th distribution, developed by *Gautheron et al.* [2008]. Results for crystal shapes, U zoning and U/Th ratios that are characteristic of the apatites in our study, suggest that "standard" Ft correction factors of 0.62–0.84 determined for our samples severely overestimate the correction: for an 80% depleted, 30-μm-wide rim the Ft correction factor should be $\geq$0.9 and it becomes negligibly close to 1 for 90% depleted rims.

[23] We also use the forward model Decomp [*Meesters and Dunai*, 2002a, 2002b; *Dunai*, 2005] to illustrate the effect of cooling history and U-Th zoning on the AHe ages. The algorithm takes into consideration alpha ejection from the external part of the crystals and He diffusion out of the grains, both of which strongly depend on U and Th zoning. In order to assess the extent to which the age variation measured in several replicates could be due to zoning, we modeled the effect of zoning on apparent AHe ages for several realistic cooling history scenarios with rates between 8 and 25°C/Ma (Figure 9). The model apatite used is a sphere of 75 μm radius, which corresponds to the mean surface/volume ratio observed in the crystals we dated in

Table 3. AHe Dating Results[a]

Sample	^{232}Th	^{232}Th 1σ	^{238}U	^{238}U 1σ	^{4}He	^{4}He 1σ	TA Error	Raw Age	1σ Raw Age Error	L	W	Tr	F_t	Corr Age	1σ Corr Age Error	Use	WR Age	WR Error	WC Age	WC Error
Guttannen Section																				
AV28-1	0.035	0.002	0.106	0.006	1.15×10^{-10}	6.15×10^{-13}	8.6	8.3	0.7	235	150	2	0.81	10.3	0.9	A				
AV28-2	0.022	0.002	0.124	0.007	2.38×10^{-10}	1.30×10^{-12}	8.7	15.1	1.3	245	135	2	0.79	19.0	1.7	A				
AV28-3	0.071	0.005	0.116	0.007	1.23×10^{-10}	4.74×10^{-13}	8.5	7.6	0.7	200	160	1	0.82	9.3	0.8	Y				
AV28-4	0.019	0.001	0.111	0.007	1.21×10^{-10}	4.57×10^{-13}	9.1	8.6	0.8	225	145	1	0.81	10.6	1.0	Y				
AV28-5	0.024	0.002	0.110	0.006	1.51×10^{-10}	5.94×10^{-13}	8.5	10.7	0.9	225	150	2	0.80	13.3	1.1	Y	9.0	1.3	11.1	1.7
AV37-1	0.024	0.002	0.468	0.026	4.99×10^{-10}	1.85×10^{-12}	8.8	8.7	0.8	185	175	0	0.84	10.3	0.9	Y				
AV37-2	0.007	0.001	0.199	0.011	1.87×10^{-10}	7.09×10^{-13}	9.4	7.7	0.7	200	150	1	0.82	9.4	0.9	Y				
AV37-3	0.038	0.002	0.168	0.009	1.57×10^{-10}	5.85×10^{-13}	8.3	7.3	0.6	195	135	2	0.78	9.4	0.8	Y				
AV37-4	0.013	0.001	0.252	0.016	2.64×10^{-10}	1.02×10^{-12}	9.5	8.5	0.8	220	155	1	0.82	10.3	1.0	Y	8.0	0.7	9.8	0.9
AV36-1	0.048	0.003	0.102	0.006	1.05×10^{-10}	4.57×10^{-13}	8.6	7.6	0.7	265	125	2	0.78	9.8	0.8	Y				
AV36-2	0.047	0.003	0.059	0.004	5.38×10^{-11}	2.15×10^{-13}	9.5	6.3	0.6	140	65	1	0.62	10.2	1.0	Y				
AV36-3	0.026	0.002	0.073	0.005	6.75×10^{-11}	2.69×10^{-13}	9.3	7.0	0.7	170	125	2	0.76	9.2	0.9	Y				
AV36-4	0.040	0.002	0.056	0.003	5.64×10^{-11}	2.25×10^{-13}	8.3	7.1	0.6	160	130	2	0.76	9.3	0.8	Y				
AV36-5	0.140	0.008	0.109	0.006	3.27×10^{-10}	1.31×10^{-12}	8.2	18.9	1.6	215	130	2	0.78	24.4	2.0	D	7.1	0.6	9.6	0.9
AV45-1	0.009	0.001	0.228	0.013	1.39×10^{-10}	5.55×10^{-13}	8.8	5.0	0.4	155	105	2	0.73	6.8	0.6	Y				
AV45-2	0.013	0.001	0.259	0.015	1.70×10^{-10}	7.41×10^{-13}	10.0	5.3	0.5	150	100	1	0.74	7.2	0.7	Y				
AV45-3	0.010	0.001	0.213	0.011	1.26×10^{-10}	5.59×10^{-13}	9.1	4.8	0.4	215	70	0	0.67	7.2	0.7	Y				
AV45-4	0.013	0.001	0.182	0.010	1.03×10^{-10}	4.55×10^{-13}	9.9	4.6	0.5	150	75	0	0.68	6.7	0.7	Y				
AV45-5	0.018	0.001	0.256	0.014	1.92×10^{-10}	7.57×10^{-13}	9.1	6.1	0.6	175	100	1	0.74	8.2	0.7	Y	5.2	0.5	7.2	0.7
AV48-1	0.016	0.001	1.086	0.058	8.48×10^{-10}	3.18×10^{-12}	9.1	6.4	0.6	200	150	2	0.80	8.0	0.7	Y				
AV48-2	0.007	0.001	0.664	0.035	4.59×10^{-10}	1.80×10^{-12}	8.8	5.7	0.5	185	125	2	0.77	7.4	0.7	Y				
AV48-3	0.006	0.000	0.407	0.023	2.68×10^{-10}	1.07×10^{-12}	9.0	5.4	0.5	190	125	1	0.79	6.9	0.6	Y				
AV48-4	0.011	0.001	0.870	0.050	6.56×10^{-10}	2.61×10^{-12}	9.3	6.2	0.6	210	170	0	0.84	7.3	0.67	Y				
AV48-5	0.026	0.002	0.312	0.018	1.63×10^{-10}	6.51×10^{-13}	8.9	4.2	0.4	190	155	1	0.82	5.1	0.5	Y	5.9	0.5	7.4	0.7
Formazza Section																				
AV12-1	0.016	0.001	0.275	0.016	5.72×10^{-12}	2.64×10^{-14}	8.7	0.2	0.0	240	150	2	0.81	0.2	0.0	D				
AV12-2	0.005	0.000	0.005	0.001	9.73×10^{-13}	4.49×10^{-15}	15.2	1.2	0.2	180	100	2	0.72	1.7	0.3	B, C				
AV12-3	0.000	0.000	0.005	0.001	4.82×10^{-12}	2.22×10^{-14}	32.1	7.4	2.4	225	140	2	0.80	9.3	3.0	C				
AV12-4	0.032	0.002	0.033	0.002	1.47×10^{-11}	7.02×10^{-14}	10.0	3.0	0.3	220	150	1	0.81	3.6	0.4	Y				
AV12-5	0.013	0.001	0.014	0.001	1.67×10^{-11}	6.80×10^{-14}	11.2	8.0	0.9	165	110	1	0.75	10.6	1.2	Y	5.2	2.4	6.7	3.4
AV4-1	0.121	0.007	0.108	0.007	5.84×10^{-11}	2.68×10^{-13}	8.6	3.5	0.3	160	115	1	0.76	4.6	0.4	Y				
AV4-2	0.042	0.003	0.049	0.003	2.23×10^{-11}	1.02×10^{-13}	9.6	3.1	0.3	260	185	2	0.84	3.8	0.4	Y				
AV4-3	0.054	0.004	0.054	0.003	2.01×10^{-11}	9.23×10^{-14}	8.7	2.5	0.2	235	155	2	0.81	3.1	0.3	Y				
AV4-4	0.024	0.002	0.018	0.001	7.47×10^{-12}	3.46×10^{-14}	9.0	2.6	0.2	200	160	2	0.80	3.2	0.3	Y				
AV4-5	0.031	0.002	0.030	0.002	1.74×10^{-11}	8.05×10^{-14}	9.2	3.9	0.4	275	175	1	0.84	4.6	0.4	Y	3.1	0.5	3.9	0.7
AV6-1	0.094	0.006	0.039	0.002	3.38×10^{-11}	1.54×10^{-13}	9.0	4.6	0.4	200	120	1	0.77	5.9	0.5	Y				
AV6-2	0.044	0.003	0.039	0.002	1.57×10^{-11}	7.22×10^{-14}	9.1	2.6	0.2	205	165	2	0.81	3.3	0.3	Y				
AV6-3	0.055	0.004	0.045	0.003	4.10×10^{-11}	1.87×10^{-13}	9.6	5.8	0.6	230	150	2	0.80	7.3	0.7	Y	4.3	1.3	5.4	1.7
AV13-1	0.039	0.003	0.021	0.001	9.66×10^{-12}	4.43×10^{-14}	9.7	2.6	0.3	195	175	0	0.84	3.1	0.3	Y				
AV13-2	0.002	0.000	0.001	0.000	2.52×10^{-13}	1.16×10^{-15}	23.1	1.1	0.2	250	105	0	0.76	1.4	0.3	B, C				
AV13-3	0.028	0.002	0.010	0.001	2.86×10^{-11}	8.58×10^{-14}	8.9	14.5	1.3	240	165	0	0.83	17.4	1.6	A, C				
AV13-4	0.129	0.008	0.068	0.004	3.09×10^{-11}	1.41×10^{-13}	8.9	2.6	0.2	260	85	2	0.69	3.7	0.3	Y	2.6	0.2	3.4	0.3

[a]The ^{232}Th, ^{238}U, mass of Th and U in the grain (ng) and corresponding 1σ analytical error (ng); ^{4}He, volume of He extracted (cm^3), in standard laboratory conditions and corresponding 1σ analytical error (cm^3); TA error, total analytical error (%) calculated from the 1σ analytical errors on ^{232}Th, ^{238}U and ^{4}He; Raw age: grain age before applying the F_t alpha-ejection correction factor (Ma); 1σ age err: analytical error on raw age (Ma); L and W, length and width of crystal (μm); Tr, number of intact crystal terminations; F_t: alpha correction factor [*Farley*, 2002]; Corr age: grain age after dividing the raw age by the F_t alpha ejection correction factor (Ma); 1σ age error, analytical error on corrected age (Ma); Use, use of a replicate age in the calculation of uncertainty-weighted age (Y), or reason for discarding the replicate before uncertainty-weighted age calculation. These reasons include A, He extraction at second heating amounting to more than 5% of the extraction at first heating (suggesting the presence of He-rich inclusion); B, blank level He extraction at first heating; C, ICP-MS isotopic counts per second smaller than our limit of quantification (10 times the number of counts per second measured with ultrapure 5 M HNO_3 blank); D, a single replicate age is close to zero (suggesting the presence of a U-rich inclusion), or in samples with more than three valid replicates: a $\pm2\sigma$ confidence interval around the raw age is isolated from every other valid replicate; WR age, analytical uncertainty-weighted raw age (Ma); WR error, weighted 1σ standard deviation or average 1σ analytical error, whichever is highest, on weighted raw age (Ma); WC age, analytical uncertainty-weighted-corrected age (Ma); WC error, weighted 1σ standard deviation or average 1σ analytical error, whichever highest, on weighted-corrected age (Ma). Samples are ranked in decreasing elevation order.

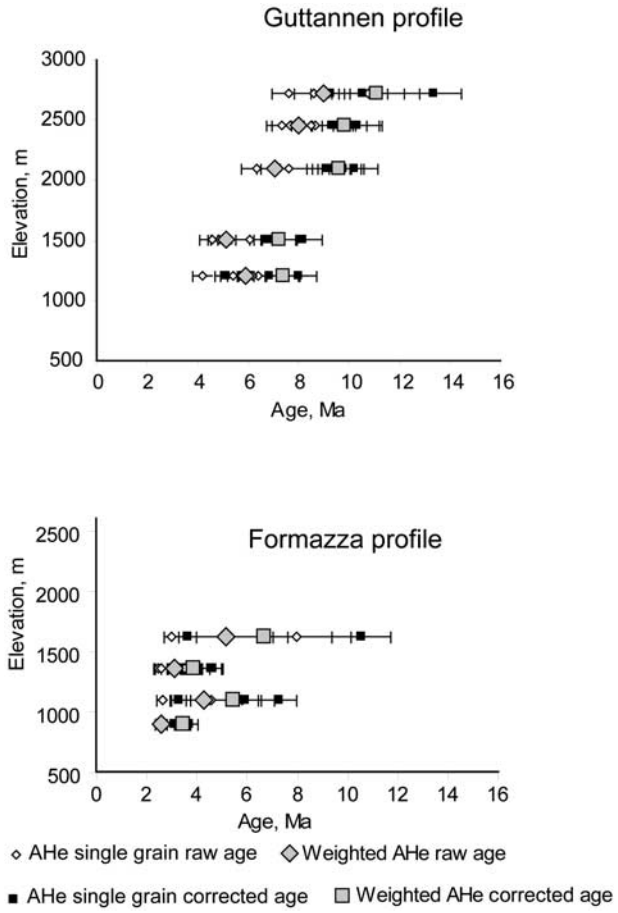


Figure 5. Spread of single-grain uncorrected (white diamonds) and corrected (black squares) AHe ages with 1σ analytical uncertainty, compared to weighted-average AHe ages (weighted according to 1σ analytical uncertainty; gray diamonds and squares, respectively, with error bars as explained in Table 3) for the Guttannen and Formazza elevation profiles.

this study. The emission distance was set at 20 μm, the activation energy at 8.65 kJ/mol and D_0 at 1807.8 cm^2/s.

[24] In the conditions tested, the apparent age of zoned apatites varies between −30.8% and +49.7% of the age calculated for unzoned apatites (Table 4 and Figure 9). The model confirms that apatites with a strong internal zoning of U and Th (cases D and E) may have apparent ages that are much older than under the assumption of no zoning, and therefore do not require application of an alpha ejection correction. The dependency of age on U-Th zoning might explain the overlap between AFT and AHe ages exposed in Figure 7.

5. Qualitative Interpretation of Age-Elevation Relationships

[25] All AFT and AHe ages obtained on the Guttannen and the Formazza elevation profiles are plotted in Figure 7, including AFT samples with multiple grain age populations. The comparison between AFT central ages, raw and alpha-ejection-corrected AHe ages in the Guttannen elevation profile (Figure 7) shows that uncorrected AHe ages are generally slightly younger than AFT ages, but the corrected AHe ages are older. The similarity of the AFT and AHe ages and the steepness of the age-elevation relationships in the Guttannen profile (Figure 7) suggest that rapid cooling, and therefore exhumation, occurred around 9–7 Ma.

[26] On the Guttannen profile, the elevation of the zero age intersect of the AFT age-elevation regression line lies ~6000 m below sea level (Figure 4), i.e., at least 7150 m below the valley bottom. Assuming a 20–30°C/km geothermal gradient [*Kohl*, 1999], the temperature at this depth is 140 to 210°C. This is clearly above the closure temperature for the AFT system, requiring that the cooling rate of the Aar Massif has slowed since ~7 Ma, which is the approximate AFT age of the lowest samples displaying a

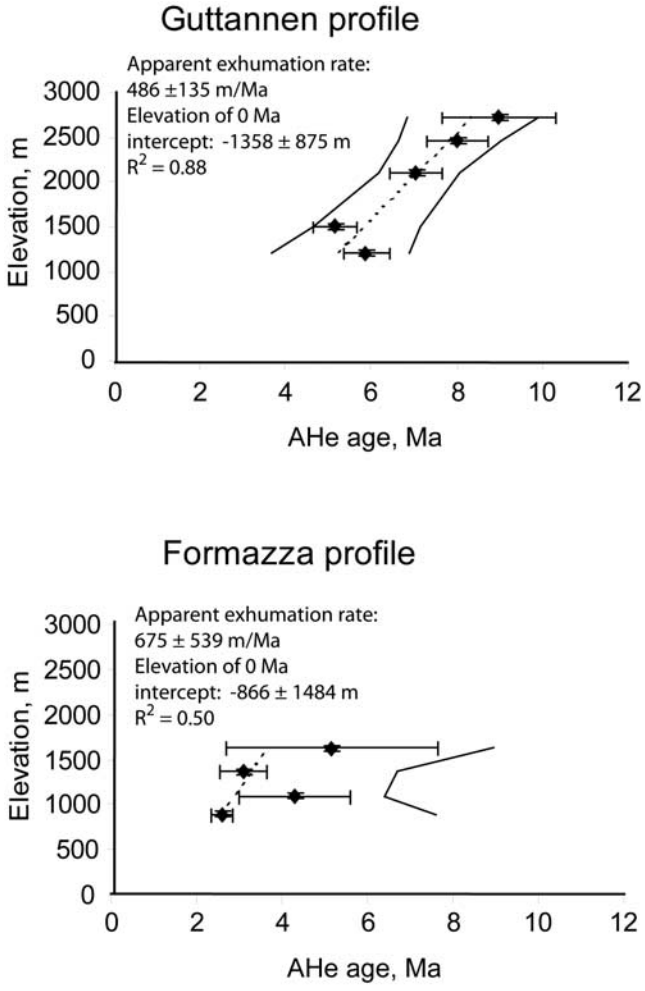


Figure 6. AHe age-elevation profiles and weighted regression relationship (dashed line, regression line; bold lines, 95% confidence interval) for the Guttannen and the Formazza areas. Weighted-average-uncorrected AHe ages were used, with error bars as explained in Table 3.

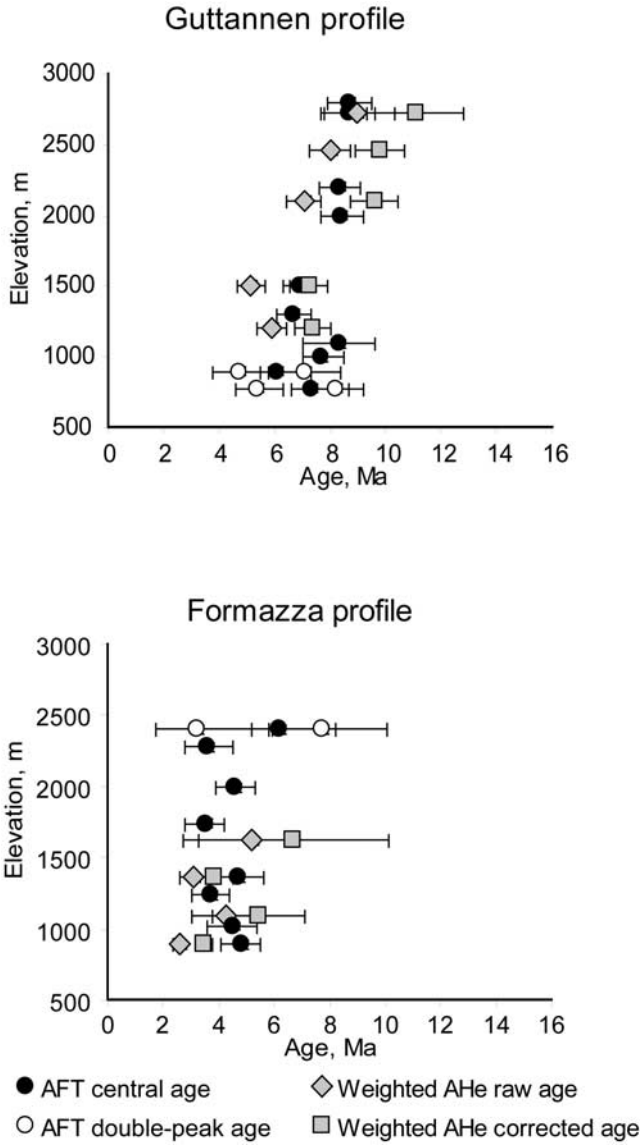


Figure 7. Comparison of AFT ages (circles, 1σ error bars) with uncorrected (diamonds) and alpha-ejection-corrected (squares) 1σ analytical uncertainty-weighted average AHe ages (with error bars as explained in Table 3), obtained in the Guttannen and the Formazza elevation profiles. White circles are used in addition to the black symbols showing central age, in samples where single-grain AFT ages are dispersed and can be characterized as belonging to several age populations, each grouping at least 30% of dated grains.

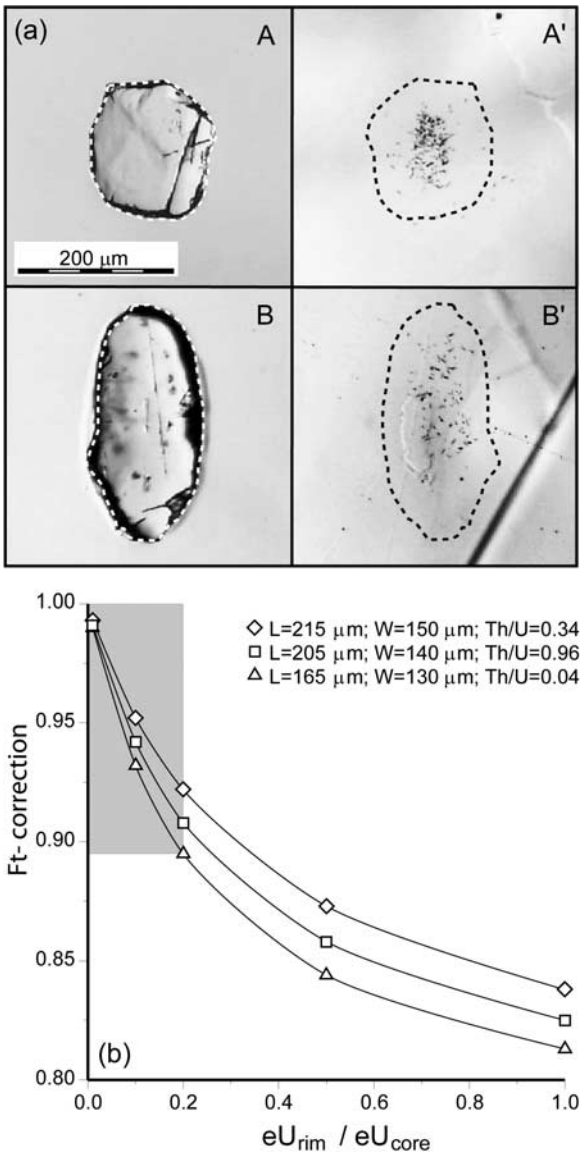


Figure 8. (a) Two examples of internal U zoning in apatites dated in this study, as recorded by the distribution of induced track in mica detectors used for AFT dating (A and A′, sample AV4; B and B′, sample AV2). The area covered by induced fission tracks in the mica detector (A′, B′) is clearly smaller than the polished area of the corresponding crystals (A, B). Dashed lines indicate the grain contour. In both cases, the outer U-poor layer is 30–40 μm thick. (b) Predicted Ft correction factor from a Monte Carlo model of He ejection [*Gautheron et al.*, 2008] for different crystal sizes (length L, width W), Th/U ratios (provided in key) and U depletion in a 30 μm wide rim (eU_{rim}/eU_{core}, with eU the effective uranium concentration as in the work by *Shuster et al.* [2006]). Grain sizes, Th/U ratios, and rim widths are characteristic of samples in this study. Shaded box corresponds to inferred range of Ft corrections applicable to our samples (compare to "standard" Ft correction for unzoned apatite; $eU_{rim}/eU_{core} = 1$).

single age population in the profile. The presence of two samples with multiple age populations at the base of the profile (open circles in Figure 7) is consistent with this interpretation as they may result from a slower passage of the partial annealing zone after ~7 Ma, dispersing the ages of individual grains.

[27] The AHe age-elevation relationship shows a zero age intercept at ~1350 m below sea level (Figure 6), i.e., at least 2350 m below the valley bottom, where we expect temper-

atures of 45–70°C. This is undistinguishable from the He closure temperature in rapidly cooling apatites and therefore does not require a change in exhumation rate since ~9 Ma (the highest AHe age in the elevation profile), in contrast to the AFT data above. There is a contradiction between the two exhumation scenarios interpreted from the depth of the zero age intersects of the AFT and AHe age-elevation

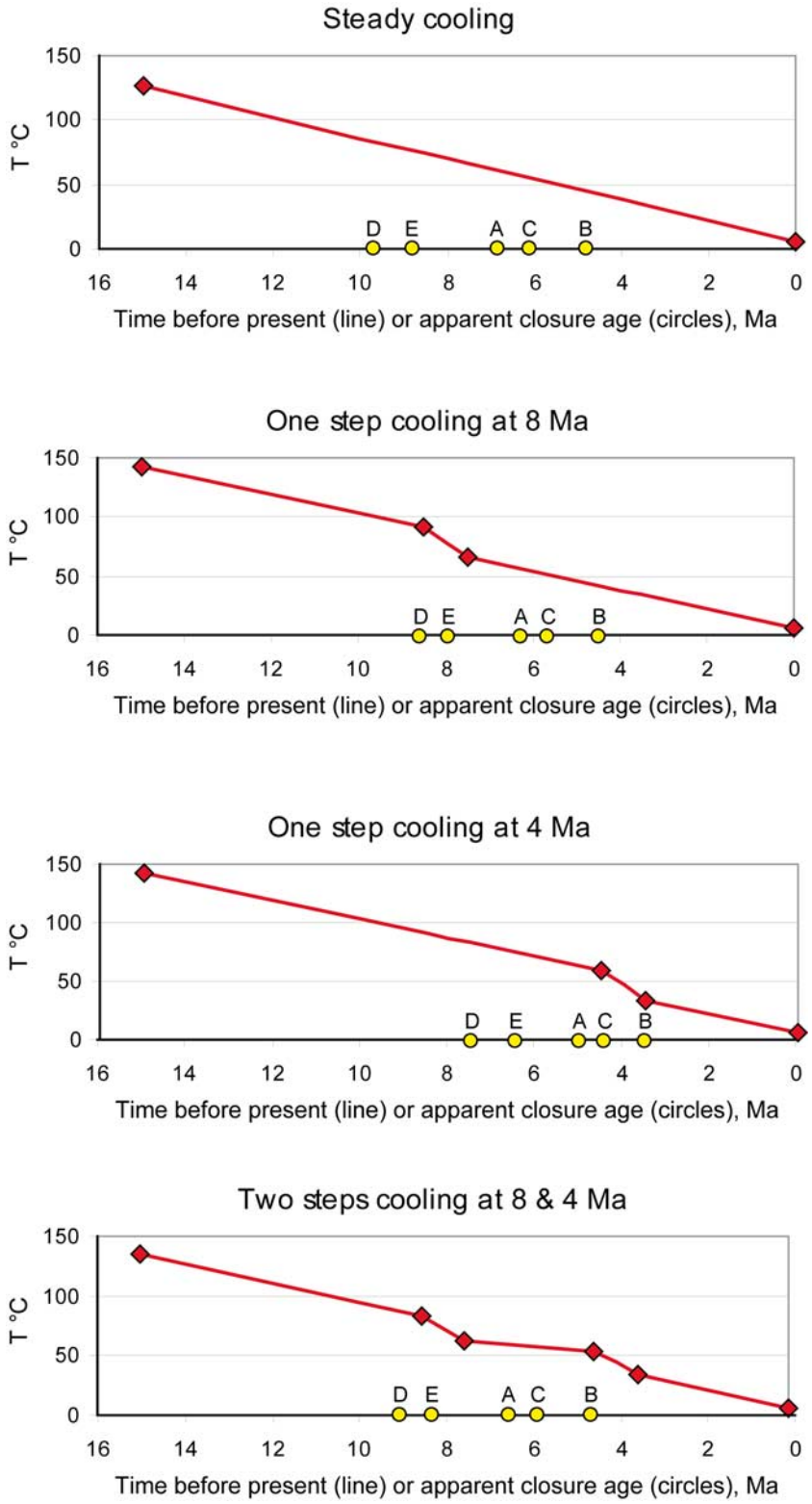


Figure 9

Table 4. Comparison Between Decomp Modeled AHe Ages for Different Cooling Scenarios[a]

	A	B (% A)	C (% A)	D (% A)	E (% A)
Steady cooling rate	6.8	4.8 (−29.8)	6.1 (−10.6)	9.7 (+41.7)	8.8 (+28.4)
Faster cooling at 8 Ma	6.3	4.5 (−28.4)	5.7 (−9.7)	8.6 (+37.1)	8.0 (+27.1)
Faster cooling at 4 Ma	5.0	3.4 (−30.8)	4.4 (−11.7)	7.4 (+49.7)	6.4 (+29.3)
Faster cooling at 8 and 4 Ma	6.5	4.7 (−28.7)	5.9 (−9.9)	9.0 (+38.2)	8.3 (+27.4)

[a]Each period of faster cooling lasts for 1 Ma, centered on the age indicated (see Figure 9). A (Ma): apparent age for nonzoned apatites (Ma), B and C, apparent age and age difference (in % of age A) in two cases of external zoning; D and E, apparent age and age difference (in % of A) in two cases of internal zoning. Details on B–E zoning are given in Figure 9 caption.

regression lines, which can tentatively be explained by the relatively high age uncertainties.

[28] On the Formazza profile, the low number and the relative dispersion of AHe data do not enable us to use the AER with confidence (Figure 6). The uncorrected AHe ages are generally in the same range as AFT ages, but corrected AHe ages are slightly older (Figure 7). The observation of a sample with two AFT age populations at the top of the profile may result from a relatively slow passage of the partial annealing zone prior to ~5 Ma, having caused individual apatite ages to disperse. The overlapping AFT and AHe ages in Formazza, together with the steep to negative AER and the presence of a sample with dispersed individual grains age at the top of the profile might result from a period of fast exhumation around 5–4 Ma, following a period of slower passage through the AFT partial annealing zone prior to ~5 Ma.

[29] The combination of observations in the Guttannen and the Formazza profiles suggests a common period of slow exhumation centered on 7–5 Ma, with a period of rapid exhumation before (recorded in the Guttannen profile) and after (recorded in the Formazza profile). Without higher-temperature thermochronometer data (such as zircon (U-Th)/He), we cannot assess the evidence for a similar period of rapid exhumation prior to ~7 Ma in Formazza. Given the generally younger cooling ages in the Italian profile, it is clear that the average exhumation rate since 6 Ma has been higher there than in the Swiss profile (Figure 3). Our qualitative analysis of AFT and AHe data on two elevation profiles along a N-S transect linking the Aar Massif to the Lepontine Dome thus lead us to propose the following scenario for late Neogene exhumation: a period of fast exhumation (9–7 Ma) was followed by 2 Ma of slow cooling (7–5 Ma). Subsequently, exhumation increased again (5–4 Ma), but more intensely on the southern flank of the orogen. This latest observation provides some support for the hypothesis of acceleration in alpine exhumation at ~5 Ma [e.g., *Kuhlemann*, 2000; *Cederbom et al.*, 2004; *Willett et al.*, 2006; *Vernon et al.*, 2008].

[30] If we assume that the AFT age at the top of the Formazza profile (~2400 m elevation) and the two AFT ages at the bottom of the Guttannen profile (~850 m elevation) remained for a longer time than other samples in the partial annealing zone between 7 and 5 Ma (Figure 7), and if the elevation of the partial annealing zone was comparable in both areas at the time of closure, then we infer a minimal additional exhumation of circa 1550 m during the last 5 Ma in Formazza compared to Guttannen. This is a minimum estimate, as it does not integrate the width of the partial annealing zone between its base (corresponding to the samples in Formazza) and its summit (corresponding to the samples in Guttannen).

6. Prediction and Comparison of Exhumation Histories Using Pecube

[31] In previous studies, age-elevation profiles have often been directly interpreted in terms of exhumation rates [*Michalski and Soom*, 1990; *Lihou et al.*, 1995; *Rahn et al.*, 1997] even though the slopes of age-elevation relationships might be overestimated (see section 3.1).

[32] The program Pecube solves for the thermal structure of the crust and the cooling history of rocks that are currently at the surface for arbitrary exhumation and relief histories. The version used here is based on the version of *Braun and Robert* [2005], which includes isostatic response to relief change, calculates apatite fission track and (U-Th)/He ages and compares these with input data. AFT ages are calculated using the *Green et al.* [1989] annealing model but with model parameters as recalculated by *Stephenson et al.* [2006]. (U-Th)/He ages are calculated for a spherical diffusion model within a 100 μm diameter and diffusion parameters from *Farley* [2000]. *Braun* [2002, 2003] provides detailed explanations of the thermal calculations.

Figure 9. Effect of U and Th zonation on calculated AHe ages using Decomp, for four different cooling scenarios. In each case, total cooling is ~130°C in the last 15 Ma, with times of cooling rate change underlined by a diamond. Five different cases of U and Th zonation are tested for each cooling history. A, unzoned apatite of 75 μm radius; B, externally zoned apatite with U and Th concentrated in the outer 15 μm; C, externally zoned apatite with U and Th concentrated in the outer 30 μm; D, internally zoned apatite with U and Th concentrated in the inner 30 μm; E, internally zoned apatite with U and Th concentrated in the inner 60 μm. The circles represent predicted AHe ages for these five cases of zonation; their spread underlines the large impact of zonation on apparent AHe age (see text for details on the method).

Table 5. Values of Fixed Crustal, Thermal, and Flexural Parameters Used in Pecube Runs

	Value	Reference[a]
Parameters for thermal calculation		
Model crustal thickness C	50 km	*Stampfli et al.* [1998]
Number of nodes in the vertical (z) direction nz	21	
Thermal diffusivity κ	25 km^2 Ma^{-1}	*Braun and Robert* [2005]
Temperature at the base of the model T_{max}	650°C	*Bousquet et al.* [1997]
Temperature at sea level T_0	15°C	
Atmospheric lapse rate G	6°C km^{-1}	
Crustal heat production H	8°C Ma^{-1}	*Braun and Robert* [2005]
Erosional response time τ	1000 Ma	
Parameters for plate flexure		
Crustal density ρ_c	2700 kg m^{-3}	
Sublithospheric mantle density ρ_m	3200 kg m^{-3}	
Young's modulus Y	10^{+11} Pa	
Poisson ratio ν	0.25	
Equivalent elastic thickness Te	20 km	*Burov and Diament* [1996]

[a]References are given for parameter values where appropriate.

[33] As Pecube can only be used over limited areas, where the geothermal gradient, exhumation history and thermal properties of the crust are assumed homogeneous, we limited our models to two 37 × 38 km regions, centered on the Guttannen and the Formazza profiles (locations indicated by boxes in Figure 1), using a 1 km resolution resampled version of the digital elevation model available from the CGIAR-CSI SRTM 90 m database (http://srtm.csi.cgiar.org). We tested more than 120 different exhumation and relief change scenarios in each area, fixing the thermal parameters of the crust as well as the values of flexural parameters used to include the isostatic response to relief change, as detailed in Table 5. We calculated AFT and AHe ages for each surface grid node from the predicted cooling histories and then calculated the cumulated misfit (μ) between observed and predicted ages in order to assess the likelihood of each set of parameters tested (Figure 10):

$$\mu = \sqrt{\sum_{i=1}^{n} \left(\frac{\mathrm{age}_{\mathrm{obs}} - \mathrm{age}_{\mathrm{pred}}}{\sigma_{\mathrm{age}_{\mathrm{obs}}}} \right)^2}, \qquad (1)$$

where $\mathrm{age}_{\mathrm{obs}}$ and $\mathrm{age}_{\mathrm{pred}}$ are the observed and predicted ages, respectively, and $\sigma_{\mathrm{age}_{\mathrm{obs}}}$ is the uncertainty on the observed age. For the misfit calculation we used either central AFT ages or the main age peak component in cases where it included more than 70% of the grains counted (see Table 2); otherwise the age was not used. The AHe ages used in the model were not corrected for alpha ejection, due to presumed U and Th zoning susceptible to cause overestimation of the correction factor.

[34] We performed Pecube runs for four types of exhumation scenarios characterized by either a constant exhumation rate, one or two temporary exhumation pulses, or a single step of exhumation increase (Figures 11–14). Every model was run over a period long enough to exhume 6000 m of material, to ensure that the material exposed at the surface at the final stage was located deeper than the AFT partial annealing zone at the onset of the model run. Relief evolution is defined by a factor β defined for each time step, such that at that time step, the elevation difference between any pixel in the model and the maximum elevation equals β times the present-day value. We tested scenarios in which relief increased ($\beta < 1$) or decreased ($\beta > 1$) homogeneously or stepwise through time, as well constant relief scenarios ($\beta = 1$).

[35] Our first set of runs tested different rates of constant exhumation and either steady relief or continuously increasing (initial $\beta = 0.4$) or decreasing (initial $\beta = 1.6$) relief (Figure 11). In the Formazza area, the best fitting scenario (cumulated misfit $\mu = 4.4$, case B in Figures 11 and 15) is obtained for 750 m/Ma (insensitive to relief change), and in the Guttannen area (cumulated misfit: $\mu = 7.4$, case A in Figures 11 and 15) for 400 m/Ma (with increasing relief corresponding to valley deepening). However, some of the other scenarios tested provided slightly better misfit values in Guttannen.

[36] We subsequently tested models including a single 2-Ma exhumation pulse, centered at either 8 or at 4 Ma (see color code on Figure 12). We tested different scenarios of exhumation rate variation (i-1, moderate; i-2, strong; i-3, extreme) and either steady relief, continuous relief reduction from $\beta = 1.5$, continuous relief increase from $\beta = 0.5$, or a temporary increase to $\beta = 1.5$ during exhumation pulses. In Guttannen, best fits are obtained for a pulse in exhumation rate centered at 4 Ma, with steadily or temporarily increasing

Figure 10. Comparison between two AFT age Pecube predictions in the Formazza area, with either (a) a high total misfit value of 13.3 or (b) a low misfit value of 4.2. The two scenarios have constant exhumation rates of 500 and 750 m/Ma, respectively; both have constant relief throughout the run. The color scale on the maps corresponds to Pecube-predicted ages on 1 × 1 km pixels, while the dots show measured AFT ages, with the same color code. The age-elevation insets show the superposition of the measured AFT ages (black squares with 1σ error bars) and the ages predicted at the same locations by the Pecube model (open squares). Note that all samples within the Formazza area are plotted here; not only those from the elevation profile presented in Figure 4.

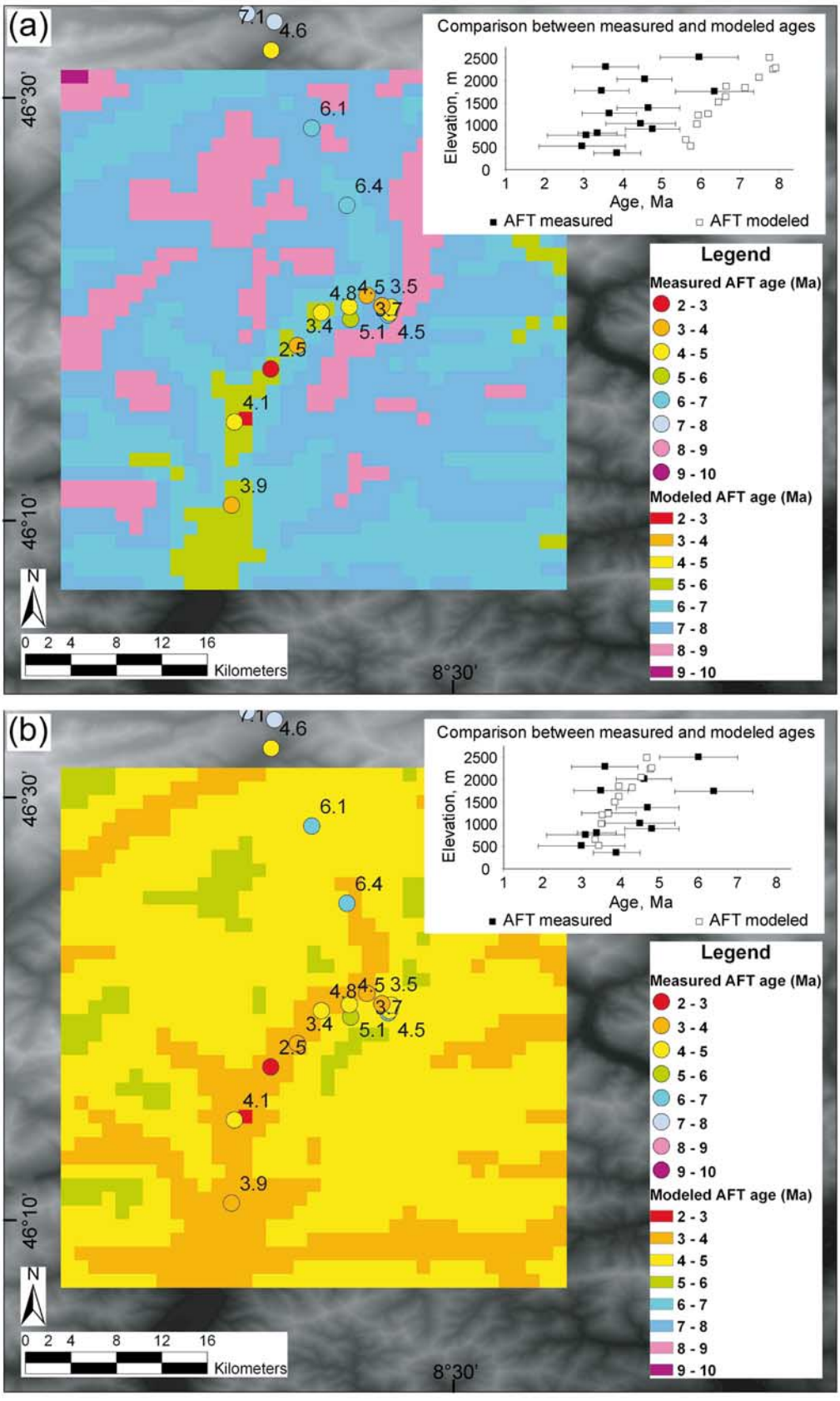

(a)
(b)
Comparison between measured and modeled ages
Elevation, m
Age, Ma
AFT measured
AFT modeled
Legend
Measured AFT age (Ma)
Modeled AFT age (Ma)
2 - 3
3 - 4
4 - 5
5 - 6
6 - 7
7 - 8
8 - 9
9 - 10
7.1
4.6
6.1
6.4
4.8
4.5
3.5
3.7
3.4
5.1
4.5
2.5
4.1
3.9
46°30'
46°10'
8°30'
N
0 2 4 8 12 16
Kilometers

Figure 10

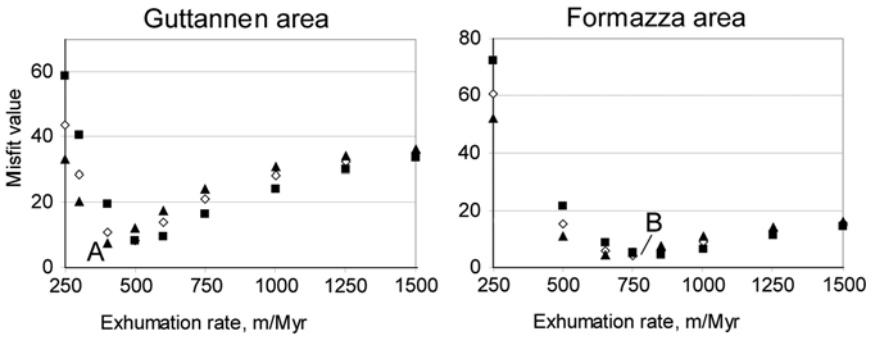


Figure 11. Cumulated misfit between predicted and measured AFT and AHe ages in the Guttannen and the Formazza study areas for different values of steady exhumation rate (plotted on x axis) and relief variation. Diamonds, steady relief; squares, relief reduction from $\beta = 1.6$ to 1; triangles, relief increase from $\beta = 0.4$ to 1. A ($\mu = 7.4$) and B ($\mu = 4.4$) refer to cases A and B in Figure 15. See text for details on the method.

relief. The scenarios with an extreme variation in exhumation rate (100 to 1000 m/Ma during the pulses) illustrate the important role played by relief change when the background exhumation rate is very low (100 m/Ma). In Formazza, we observe a broadly similar pattern although the scarcity of AFT and AHe ages older than 6 Ma in this profile does not allow us to accurately test models involving an exhumation pulse centered at 8 Ma. In both areas, relatively high misfit values ($\mu = 8.4$ and 16.2, respectively, for the best fit) led us to discard scenarios involving a single exhumation pulse.

[37] Third, we tested models that included two exhumation pulses, both lasting for 2 Ma and centered at 8 and

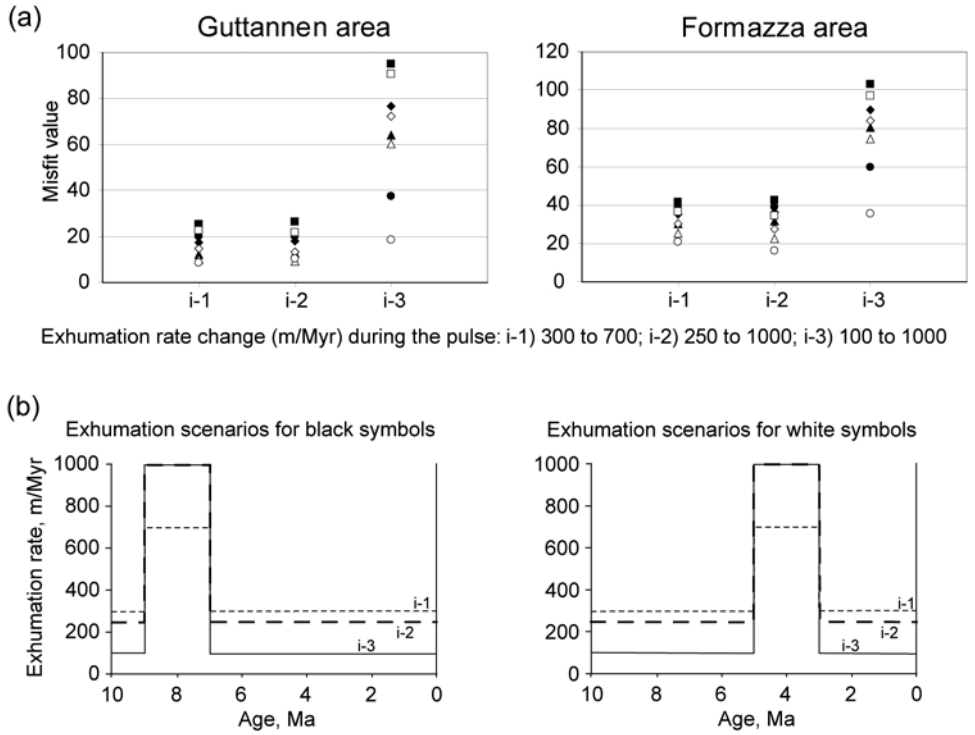


Figure 12. (a) Cumulated misfit between predicted and measured AFT and AHe ages in the Guttannen and the Formazza study areas, for different intensities (i-1, i-2, i-3) of 2-Ma-long exhumation pulses centered at either 8 Ma (black) or 4 Ma (white) and a choice of relief variation. Diamonds, steady relief; squares, relief reduction from $\beta = 1.5$ to 1; triangles, relief increase from $\beta = 0.5$ to 1; circles, temporary relief increase from $\beta = 1$ to 1.5 during exhumation pulses. See text for further details on the method. (b) Illustration of the 6 different exhumation rate scenarios tested, centered at 8 or 4 Ma and with i-1, i-2, or i-3 intensity variation as detailed in the legend.

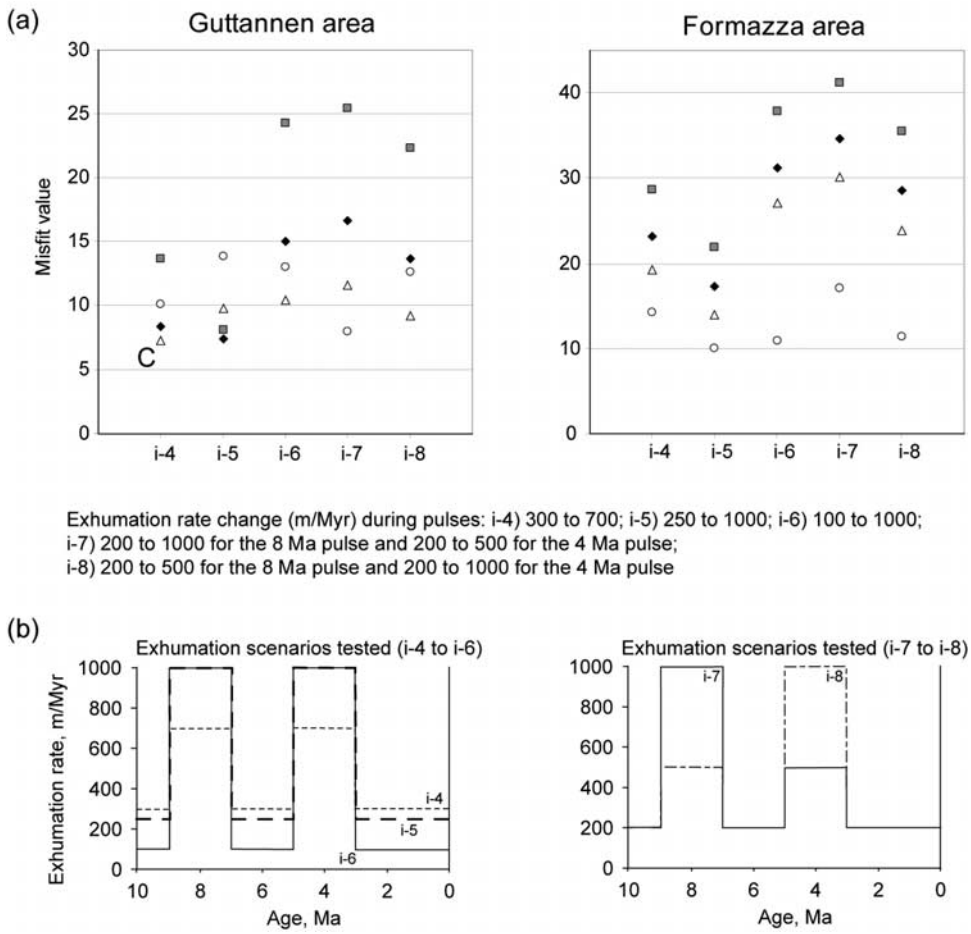


Figure 13. (a) Cumulated misfit between predicted and measured AFT and AHe ages in the Guttannen and the Formazza study areas for different intensities (i-4, i-5, i-6, i-7, i-8) of two 2-Ma-long exhumation pulses centered at 8 and 4 Ma and a choice of relief variation. Diamonds, steady relief; squares, relief reduction from $\beta = 1.5$ to 1; triangles, relief increase from $\beta = 0.5$ to 1; circles, temporary relief increase from $\beta = 1$ to 1.5 during exhumation pulses. See text for further details on the method. C ($\mu = 7.2$) refers to case C in Figure 15. (b) Illustration of the five different exhumation rate scenarios tested, with i-4, i-5, i-6, i-7, or i-8 intensity variation centered at 8 or 4 Ma as detailed in the legend.

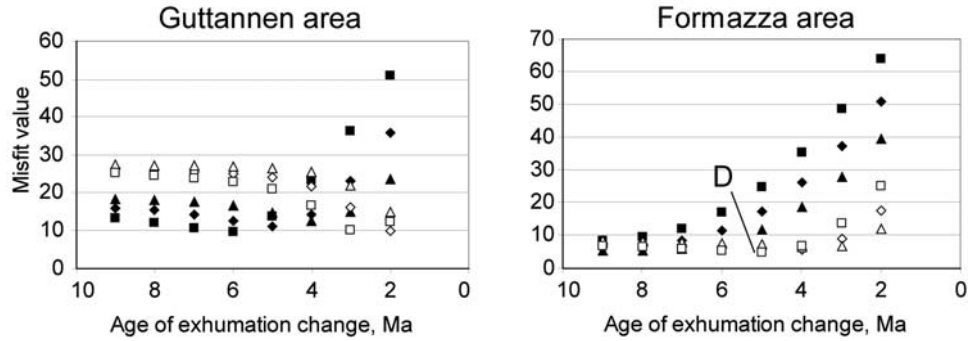


Figure 14. Cumulated misfit between predicted and measured AFT and AHe ages in the Guttannen and the Formazza study areas for different scenarios of single-step exhumation rate increase occurring at the age indicated on the *x* axis, with different intensities (200 to 700 m/Ma in black, or 300 to 1000 m/Ma in white) and a choice of relief variation. Diamonds, steady relief; squares, relief reduction from $\beta = 1.3$ to 1; triangles, relief increase from $\beta = 0.7$ to 1. See text for further details on the method. D ($\mu = 4.8$) refers to case D in Figure 15.

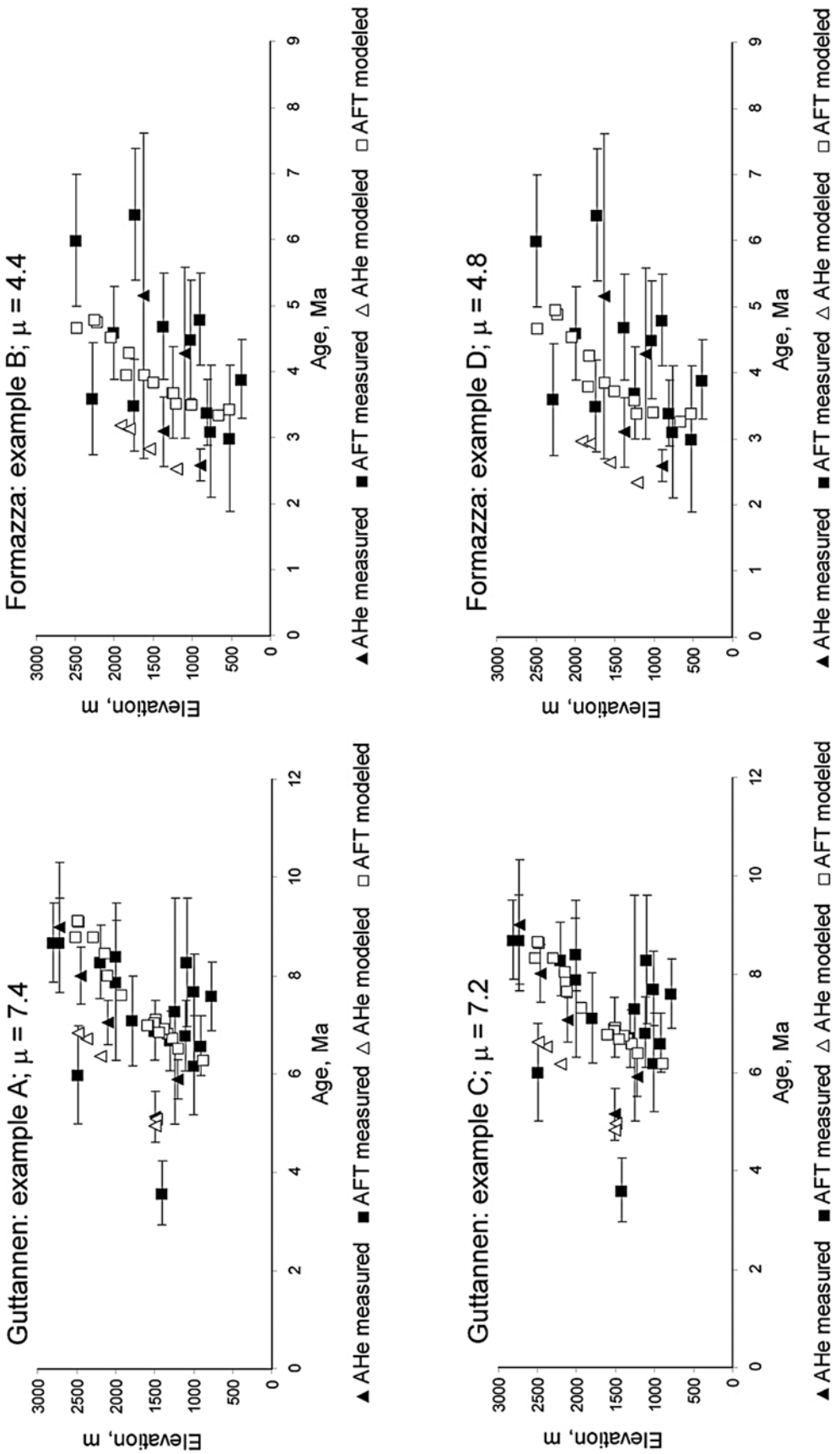


Figure 15. Comparison between measured AHe and AFT ages (closed symbols, with error bars as expressed in Tables 2 and 3) and ages predicted by Pecube modeling (open symbols); μ is the value of cumulated misfit used to quantify the difference between measured and predicted ages (see equation (1)). Examples A and C correspond to the two best fit models for Guttannen (see Figures 11 and 13), and examples B and D correspond to the best fit models for Formazza (see Figures 11 and 14). Note that all AFT and AHe ages within the model domains are plotted here, not only those from the Guttanen and Formazza elevation profiles.

4 Ma, respectively (Figure 13). The first three exhumation scenarios tested (i-4 to i-6) involve two exhumation pulses of equal importance, whereas the two last scenarios (i-7 and i-8) test exhumation pulses that differ in intensity. The relief conditions were either steady, continuously decreasing from $\beta = 1.5$, continuously increasing from $\beta = 0.5$, or increasing temporarily to $\beta = 1.5$ during exhumation pulses. In Guttannen, the best fitting scenario (cumulated misfit $\mu = 7.2$) is obtained for a moderate increase in exhumation rate (300 to 700 m/Ma) during two periods (9–7 and 5–3 Ma), in a context of increasing relief. However, another scenario with constant relief and a stronger contrast in exhumation rates (250 to 1000 m/Ma) yields an almost equally good misfit value ($\mu = 7.4$), underlining the low resolution we have to precisely quantify variations in exhumation rate. In contrast, relief change can have a strong effect, such that most scenarios involving relief decrease (squares) yield very high misfit values. The best fit scenario modeled in Guttannen (case C in Figures 13 and 15) constitutes a quantitative validation of the observations made qualitatively on AFT and AHe elevation profiles in Guttannen and Formazza (section 5 and Figure 7): an exhumation rate slower between 7 and 5 Ma than immediately before and after. Although high misfit values ($\mu \geq 10$) are obtained in Formazza for models with two exhumation pulses, they do not allow us to reject this hypothesis because, as detailed in the previous paragraph, the age distribution does not allow a good resolution on events older than 6 Ma.

[38] Finally, we tested two different intensities of single-step change in exhumation rate occurring between 9 and 2 Ma, with faster exhumation lasting until present (Figure 14). The relief conditions were either constant, increased from $\beta = 0.7$ since the exhumation rate increase or decreased from $\beta = 1.3$ over the same period. Misfit values obtained in Guttannen for such scenarios are clearly larger than misfits obtained for other scenarios ($\mu \geq 9.7$). In Formazza, however, a low misfit value ($\mu = 4.8$, case D in Figures 14 and 15) is obtained for an increase in exhumation rate from 300 to 1000 m/Ma at ~5 Ma, with little effect of tested relief changes.

7. Discussion

[39] The qualitative interpretation of age-elevation relationships led us to propose that the late Neogene denudation history of the central Alps is characterized by two distinct episodes of high exhumation rate, the first between 9 and 7 Ma recorded in the Aar Massif, and the second between 5 and 3 Ma recorded in the Lepontine Alps. A recent study in the Mont Blanc Massif [*Glotzbach et al.*, 2008] described two periods of rapid exhumation, before 6 Ma and after 3 Ma, thus proposing a three-phase scenario comparable to the qualitative interpretation of our elevation profiles (although with a slightly different timing).

[40] The numerical modeling scenario leading to the lowest misfit value in Guttannen (case C in Figures 13 and 15) supports the qualitative interpretation of elevation profiles detailed above. However, the fact that a steady exhumation scenario with valley deepening (case A in Figures 11 and 15) leads to practically the same misfit suggests that either the ages in the Guttanen area do not resolve these pulses of exhumation with sufficient resolution, or that such pulses do not exist. In Formazza, the same conclusion is reached with two scenarios of either steady exhumation rate (case B in Figures 11 and 15), or exhumation rate increase since ~5 Ma (case D in Figures 14 and 15) yielding similar misfit values. The former scenario is in agreement with detrital FT data that have been argued to show exhumational steady state in the Lepontine area since at least 20 Ma at rates of ~700 m/Ma [*Bernet et al.*, 2001; *Garzanti and Malusà*, 2008]. Taken together, the best fitting models in Guttannen and Formazza do not support a common two-phase exhumation history affecting the two study areas and more generally the Western Alps. Nevertheless, we are unable to delineate unambiguously the late Neogene exhumation history in these two areas, based on available AFT and AHe ages. A higher number of age data spanning a longer period (possibly including higher-temperature thermochronometers), combined with a more rigorous exploration of the parameter space using an inverse approach [e.g., *Braun and Robert*, 2005] would enable to determine the best fit scenarios with more accuracy.

[41] Our observations only give partial support to *Cederbom et al.*'s [2004] hypothesis of a major pulse of exhumation in the axial chain since 5 Ma, facilitated by a change to a more erosive climate. Our conclusions provide support, albeit ambiguous, for a temporal signal of increased exhumation since circa 5 Ma, which appears to be a widespread phenomenon in the Alps [*Vernon et al.*, 2008]. However, *Cederbom et al.* [2004] predicted that 6500 m of exhumation of the chain axis was necessary to trigger the observed >1400 m of flexural isostatic rock uplift and denudation in the foreland. In contrast, post-5 Ma exhumation in Guttannen and Formazza, as predicted by our four best fit models reached 2000 to 2300 m and 3750 to 5000 m, respectively. The discrepancy with *Cederbom et al.*'s [2004] prediction, however, is possibly due to the their use of a simplified isostatic rebound calculation; further 2-D flexural isostatic modeling that integrates the change in the distributed load accounting for erosion in the axial zones and the foreland basin itself is required to fully assess the significance of these numbers.

8. Conclusions

[42] Our new thermochronology data from the central European Alps enables us to draw the following conclusions:

[43] 1. Alpha-ejection-corrected AHe ages are in many cases older than AFT ages in our study. This problem might be partly explained by our observation of internally zoned induced fission tracks on external detectors used for AFT dating. Higher concentrations of radiogenic elements in the core of apatite crystals would lead to an overcorrection of AHe ages by the F_t correction factor.

[44] 2. A first approach of data analysis based on the qualitative interpretation of the two elevation profiles suggests a common suite of events for our two study areas, albeit involving different amounts of post-5 Ma exhumation. In

both the Guttannen (Aar Massif) and the Formazza (Lepontine Dome) areas, two periods of rapid exhumation at 9–7 Ma (documented in Guttannen) and 5–3 Ma (documented in Formazza) would be separated by a 7–5 Ma period of slow exhumation through the AFT partial annealing zone.

[45] 3. Numerical modeling predictions of AFT and AHe ages for several exhumation and relief change scenarios only give partial support to the above hypothesis in Guttannen, where one of the two best fitting scenarios involves an increase in exhumation rates from 300 to 700 m/Ma at 9–7 Ma, followed by a second pulse at 5–3 Ma, during relief increase. However, another best fitting scenario in Guttannen involves a constant 400 m/Ma exhumation rate with valley deepening. In Formazza, the models favor either exhumation at a constant rate of 750 m/Ma, or an exhumation rate increasing from 300 to 1000 m/Ma at ~5 Ma and constant since then, with little effect of relief change. As a result, the exhumation histories in Guttannen and Formazza appear clearly different, in contradiction with the qualitative interpretation provided above. Our results underline the weakness of exhumation scenarios borne exclusively by the interpretation of the slope of age-elevation profiles. It also stresses the potential of methods enabling testing a higher number of randomly chosen sets of exhumation, thermal and flexural parameters.

[46] 4. AFT ages along a N-S profile stretching across the central Alps are significantly older in the Aar Massif than in the western Lepontine Dome area (circa 7 Ma versus 4 Ma). According to the difference in elevation of a ~6 Ma partial annealing zone between the two profiles, the excess of denudation in the southern part of the transect reaches more than ~1550 m.

[47] 5. A similar number of at least 1450 m of differential exhumation is obtained from the estimates of exhumation since 5 Ma according to the four exhumation scenarios yielding the lowest misfit values in Pecube tests; 2000 to 2300 m in Guttannen and 3750 to 5000 m in Formazza. These values are significantly lower than the 6500 m of denudation over the axial chain, calculated by *Cederbom et al.* [2004] as required to explain the Pliocene exhumation of the Swiss Molasse basin by flexural isostatic rebound. The difference may arise from underestimation of the European plate elastic thickness in the flexural isostatic modeling performed by these authors, and/or a rather unsophisticated treatment of the modified load distributions.

[48] 6. The documentation of strong spatial variations in the amount of exhumation since 5 Ma between different massifs of the northern Western Alps suggests a localization of controls on erosion during Pliocene times. These controls may arise from either localized tectonic activity driving rock uplift, variable changes in precipitation, or variations in the rock strength of the eroded column. Whichever possibility, erosion of the Alpine orogen since 5 Ma has been spatially variable.

[49] **Acknowledgments.** Meinert Rahn contributed to sampling strategy. We thank Charlotte Cederbom and Jean-Daniel Champagnac for insightful discussions on alpine uplift and exhumation. Valérie Olive made the ICP-MS measurements, and Cécile Gautheron performed Monte Carlo modeling of He ejection presented in Figure 8. Reviewers Frédéric Herman and Sean Willett, as well as Associate Editor Todd Ehlers, provided thoughtful comments which significantly contributed to improve this manuscript. Erika Labrin, Bardhyl Muceku, and Francois Senebier provided invaluable help in preparing samples and teaching techniques to A.V. This study was supported by an INSU-CNRS "Reliefs de la Terre" program grant to P.v.d.B., a University of Edinburgh Ph.D. teaching studentship and an international student mobility (MIRA) grant of the Rhône-Alpes region to A.V.

References

Abrecht, J. (1994), Geologic units of the Aar massif and their pre-Alpine rock associations: A critical review, *Schweiz. Mineral. Petrogr. Mitt.*, *74*, 5–27.

Bernet, M., M. Zattin, J. I. Garver, M. T. Brandon, and J. A. Vance (2001), Steady-state exhumation of the European Alps, *Geology*, *29*, 35–38, doi:10.1130/0091-7613(2001)029<0035:SSEOTE>2.0.CO;2.

Bousquet, R., B. Goffé, P. Henry, X. Le Pichon, and C. Chopin (1997), Kinematic, thermal and petrological model of the central Alps: Lepontine metamorphism in the upper crust and eclogitisation of the lower crust, *Tectonophysics*, *273*, 105–127, doi:10.1016/S0040-1951(96)00290-9.

Boyce, J. W., and K. V. Hodges (2005), U and Th zoning in Cerro de Mercado (Durango, Mexico) fluorapatite: Insights regarding the impact of recoil redistribution of radiogenic ^{4}He on (U-Th)/He thermochronology, *Chem. Geol.*, *219*, 261–274, doi:10.1016/j.chemgeo.2005.02.007.

Brandon, M. T. (1992), Decomposition of fission-track grain-age distributions, *Am. J. Sci.*, *292*, 535–564.

Brandon, M. T. (1996), Probability density plot for fission-track grain-age samples, *Radiat. Meas.*, *26*, 663–676, doi:10.1016/S1350-4487(97)82880-6.

Braun, J. (2002), Quantifying the effect of recent relief changes on age-elevation relationships, *Earth Planet. Sci. Lett.*, *200*, 331–343, doi:10.1016/S0012-821X(02)00638-6.

Braun, J. (2003), Pecube: A new finite-element code to solve the 3D heat transport equation including the effects of a time-varying, finite amplitude surface topography, *Comput. Geosci.*, *29*, 787–794, doi:10.1016/S0098-3004(03)00052-9.

Braun, J., and X. Robert (2005), Constraints on the rate of post-orogenic erosional decay from low-temperature thermochronological data: Application to the Dabie Shan, China, *Earth Surf. Process. Landf.*, *30*, 1203–1225, doi:10.1002/esp.1271.

Burov, E., and M. Diament (1996), Isostasy, equivalent elastic thickness, and inelastic rheology of continents and oceans, *Geology*, *24*, 419–422, doi:10.1130/0091-7613(1996)024<0419:IEETAI>2.3.CO;2.

Cederbom, C. E., H. D. Sinclair, F. Schlunegger, and M. K. Rahn (2004), Climate-induced rebound and exhumation of the European Alps, *Geology*, *32*, 709–712, doi:10.1130/G20491.1.

Challandes, N. (2001), Comportement des systèmes isotopiques 39Ar-40Ar et Rb-Sr dans les zones de cisaillement: Exemples du massif de l'Aar (massif cristallins externes) et de la nappe de Suretta (Alpes centrales suisses), Ph.D. thesis, 268 pp., Univ. de Neuchâtel, Neuchâtel, Switzerland.

Choukroune, P., and D. Gapais (1983), Strain pattern in the Aar Granite (Central Alps): Orthogneiss developed by bulk inhomogeneous flattening, *J. Struct. Geol.*, *5*, 411–418, doi:10.1016/0191-8141(83)90027-5.

Davies, T. A., W. W. Hay, J. R. Southam, and T. R. Worseley (1977), Estimates of Cenozoic oceanic sedimentation rates, *Science*, *197*, 53–55, doi:10.1126/science.197.4298.53.

Dunai, T. J. (2005), Forward modeling and interpretation of (U-Th)/He ages, in *Low-Temperature Thermochronology: Techniques, Interpretations, and Applications*, *Rev. Mineral. Geochem*, vol. 58, edited by P. W. Reiners and T. A. Ehlers, pp. 259–274, Mineral. Soc. of Am., Chantilly, Va.

Dunkl, I. (2002), TRACKKEY: A Windows program for calculation and graphical presentation of fission track data, *Comput. Geosci.*, *28*, 3–12, doi:10.1016/S0098-3004(01)00024-3.

Evans, N. J., J. P. Byrne, J. T. Keegan, and L. E. Dotter (2005), Determination of uranium and thorium in zircon, apatite, and fluorite: Application to laser (U-Th)/He thermochronology, *J. Anal. Chem.*, *60*, 1159–1165, doi:10.1007/s10809-005-0260-1.

Fantoni, R., R. Bersezio, and F. Forcella (2004), Alpine structure and deformation chronology at the Southern Alps-Po Plain border in Lombardy, *Boll. Soc. Geol. Ital.*, *123*, 463–476.

Farley, K. A. (2000), Helium diffusion from apatite: General behavior as illustrated by Durango fluorapatite, *J. Geophys. Res.*, *105*, 2903–2914, doi:10.1029/1999JB900348.

Farley, K. A. (2002), (U-Th)/He dating: Techniques, calibrations, and applications, in *Noble Gases in Geochemistry and Cosmochemistry*, *Rev. Mineral. Geochem.*, vol. 47, edited by D. Porcelli, C. J. Ballentine, and R. Wieler, pp. 819–843, Mineral. Soc. of Am., Chantilly, Va.

Farley, K. A., R. A. Wolf, and L. T. Silver (1996), The effects of long alpha-stopping distances on (U-Th)/He ages, *Geochim. Cosmochim. Acta*, *60*, 4223–4229, doi:10.1016/S0016-7037(96)00193-7.

Foeken, J. P. T., F. M. Stuart, K. J. Dobson, C. Persano, and D. Vilbert (2006), A diode laser system for heating minerals for (U-Th)/He chronometry, *Geochem. Geophys. Geosyst.*, *7*, Q04015, doi:10.1029/2005GC001190.

Frey, M., and R. Ferreiro Mählmann (1999), Alpine metamorphism of the Central Alps, *Schweiz. Mineral. Petrogr. Mitt.*, *79*, 135–154.

Garzanti, E., and M. G. Malusà (2008), The Oligocene Alps: Domal unroofing and drainage development during early orogenic growth, *Earth Planet. Sci. Lett.*, *268*, 487–500, doi:10.1016/j.epsl.2008.01.039.

Gautheron, C., L. Tassan-Got, J. Barbarand, and M. Pagel (2008), Alpha-damage annealing effects on apatite (U-Th)/He thermochronometry, paper presented at 11th International Conference on Thermochronometry, Union Coll., Anchorage, Alaska, 15–19 Sept.

Gleadow, A. J. W. (1981), Fission-track dating methods: What are the real alternatives?, *Nucl. Tracks*, *5*, 3–14, doi:10.1016/0191-278X(81)90021-4.

Glotzbach, C., J. Reinecker, M. Danišík, M. Rahn, W. Frisch, and C. Spiegel (2008), Neogene exhumation history of the Mont Blanc massif, Western Alps, *Tectonics*, *27*, TC4011, doi:10.1029/2008TC002257.

Green, P. F., I. R. Duddy, G. M. Laslett, K. A. Hegarty, A. J. W. Gleadow, and J. F. Lovering (1989), Thermal annealing of fission tracks in apatite 4. Quantitative modelling techniques and extension to geological timescales, *Chem. Geol.*, *79*, 155–182.

Green, P. F., P. V. Crowhurst, I. R. Duddy, P. Japsen, and S. P. Holford (2006), Conflicting (U-Th)/He and fission track ages in apatite: Enhanced He retention, not anomalous annealing behaviour, *Earth Planet. Sci. Lett.*, *250*, 407–427, doi:10.1016/j.epsl.2006.08.022.

Hendriks, B. W. H., and T. F. Redfield (2005), Apatite fission track and (U-Th)/He data from Fennoscandia: An example of underestimation of fission track annealing in apatite, *Earth Planet. Sci. Lett.*, *236*, 443–458, doi:10.1016/j.epsl.2005.05.027.

Herman, F., J. Braun, T. J. Senden, and W. J. Dunlap (2007), (U-Th)/He thermochronometry: Mapping 3D geometry using micro-X-ray tomography and solving the associated production-diffusion equation, *Chem. Geol.*, *242*, 126–136, doi:10.1016/j.chemgeo.2007.03.009.

Homewood, P., P. A. Allen, and G. D. Williams (1986), Dynamics of the Molasse Basin of western Switzerland, in *Foreland Basins*, edited by P. A. Allen and P. Homewood, *Spec. Publ. Int. Assoc. Sedimentol.*, *8*, 199–217.

Hourigan, J. K., P. W. Reiners, and M. T. Brandon (2005), U-Th zonation-dependent alpha-ejection in (U-Th)/He chronometry, *Geochim. Cosmochim. Acta*, *69*, 3349–3365, doi:10.1016/j.gca.2005.01.024.

Hunziker, J. C., J. Desmons, and A. J. Hurford (1992), Thirty-two years of geochronological work in the central and western Alps: A review on seven maps, *Mem. Geol. Lausanne*, *13*, 59 pp.

Hurford, A. J. (1986), Cooling and uplift patterns in the Lepontine Alps, South Central Switzerland and an age of vertical movement of the Insubric fault line, *Contrib. Mineral. Petrol.*, *92*, 413–427, doi:10.1007/BF00374424.

Hurford, A. J., and P. F. Green (1983), The zeta age calibration of fission-track dating, *Chem. Geol.*, *1*, 285–317.

Keller, L. M., M. Hess, B. Fügenschuh, and S. Schmid (2005), Structural and metamorphic evolution of the Camughera-Moncucco, Antrona and Monte Rosa units southwest of the Simplon line, Western Alps, *Eclogae Geol. Helv.*, *98*, 19–49, doi:10.1007/s00015-005-1149-6.

Kohl, T. (1999), Transient thermal effects below complex topographies, *Tectonophysics*, *306*, 311–324, doi:10.1016/S0040-1951(99)00063-3.

Kuhlemann, J. (2000), Post-collisional sediment budget of circum-Alpine basins (central Europe), *Mem. Sci. Geol. Padova*, *52*, 1–91.

Lihou, J., A. Hurford, and A. Carter (1995), Preliminary fission-track ages on zircons and apatites from the Sardona unit, Glarus Alps, eastern Switzerland: Late Miocene-Pliocene exhumation rates, *Schweiz. Mineral. Petrogr. Mitt.*, *75*, 177–186.

Mancktelow, N. S., and B. Grasemann (1997), Time-dependent effects of heat advection and topography on cooling histories during erosion, *Tectonophysics*, *270*, 167–195, doi:10.1016/S0040-1951(96)00279-X.

Marquer, D., and M. Burkhard (1992), Fluid circulation, progressive deformation and mass-transfer processes in the upper crust: The example of basement-cover relationships in the External Crystalline Massifs, Switzerland, *J. Struct. Geol.*, *14*, 1047–1057, doi:10.1016/0191-8141(92)90035-U.

Marquer, D., and D. Gapais (1985), Les massifs cristallins externes sur une transversale Guttannen-Val Bedretto (Alpes centrales): Structures et histoires cinématiques, *C. R. Acad. Sci., Ser. II*, *301*, 543–546.

Meesters, A. G. C. A., and T. J. Dunai (2002a), Solving the production-diffusion equation for finite diffusion domains of various shapes. Part I. Implications for low-temperature (U-Th)/He thermochronology, *Chem. Geol.*, *186*, 333–344, doi:10.1016/S0009-2541(01)00422-3.

Meesters, A. G. C. A., and T. J. Dunai (2002b), Solving the production-diffusion equation for finite diffusion domains of various shapes. Part II. Application to cases with α-ejection and nonhomogeneous distribution of the source, *Chem. Geol.*, *186*, 347–363, doi:10.1016/S0009-2541(02)00073-6.

Meesters, A. G. C. A., and T. J. Dunai (2005), A noniterative solution of the (U-Th)/He age equation, *Geochem. Geophys. Geosyst.*, *6*, Q04002, doi:10.1029/2004GC000834.

Michalski, I., and M. Soom (1990), The Alpine thermotectonic evolution of the Aar and Gotthard massifs, central Switzerland: Fission-track ages on zircons and apatites and K-Ar mica ages, *Schweiz. Mineral. Petrogr. Mitt.*, *70*, 373–387.

Molnar, P. (2004), Late Cenozoic increase in accumulation rates of terrestrial sediment: How might climate change have affected erosion rates?, *Annu. Rev. Earth Planet. Sci.*, *32*, 67–89, doi:10.1146/annurev.earth.32.091003.143456.

O'Sullivan, P. B., and R. R. Parrish (1995), The importance of apatite composition and single grain ages when interpreting fission track data from plutonic rocks: A case study from the Coast Ranges, British Columbia, *Earth Planet. Sci. Lett.*, *132*, 213–224, doi:10.1016/0012-821X(95)00058-K.

Rahn, M. K., and B. Grasemann (1999), Fission track and numerical thermal modeling of differential exhumation of the Glarus thrust plane (Switzerland), *Earth Planet. Sci. Lett.*, *169*, 245–259, doi:10.1016/S0012-821X(99)00078-3.

Rahn, M. K., A. J. Hurford, and M. Frey (1997), Rotation and exhumation of a thrust plane: Apatite fission-track data from the Glarus thrust, Switzerland, *Geology*, *25*, 599–602, doi:10.1130/0091-7613(1997)025<0599:RAEOAT>2.3.CO;2.

Reiners, P. W., T. A. Ehlers, and P. K. Zeitler (2005), Past, present, and future of thermochronology, in *Low-Temperature Thermochronology: Techniques, Interpretations, and Applications*, *Rev. Mineral. Geochem.*, vol. 58, edited by P. W. Reiners and T. A. Ehlers, pp. 1–18, Mineral. Soc. of Am., Chantilly, Va.

Scardia, G., G. Muttoni, and D. Sciunnach (2006), Subsurface magnetostratigraphy of Pleistocene sediments from the Po Plain (Italy): Constraints on rates of sedimentation and rock uplift, *Geol. Soc. Am. Bull.*, *118*, 1299–1312, doi:10.1130/B25869.1.

Schaer, J. P., G. M. Reimer, and G. A. Wagner (1975), Actual and ancient uplift rate in the Gotthard region, Swiss Alps: A comparison between precise levelling and fission-track apatite age, *Tectonophysics*, *29*, 293–300, doi:10.1016/0040-1951(75)90154-7.

Schmid, S. M., O. A. Pfiffner, N. Froitzheim, G. Schönborn, and E. Kissling (1996), Geophysical-geological transect and tectonic evolution of the Swiss–Italian Alps, *Tectonics*, *15*, 1036–1064, doi:10.1029/96TC00433.

Schmid, S. M., B. Fügenschuh, E. Kissling, and R. Schuster (2004), Tectonic map and overall architecture of the Alpine orogen, *Eclogae Geol. Helv.*, *97*, 93–117, doi:10.1007/s00015-004-1113-x.

Shuster, D. L., R. M. Flowers, and K. A. Farley (2006), The influence of natural radiation damage on helium diffusion kinetics in apatite, *Earth Planet. Sci. Lett.*, *249*, 148–161, doi:10.1016/j.epsl.2006.07.028.

Spencer, A. S., B. Kohn, A. Gleadow, M. Norman, D. Belton, and T. Carter (2004), The importance of residing in a good neighbourhood: Rechecking the rules of the game for apatite (U-Th)/He thermochronometry, paper presented at 10th International Conference on Fission Track Dating and Thermochronology, Amsterdam, Netherlands.

Stampfli, G. M., J. Mosar, D. Marquer, R. Marchant, T. Baudin, and G. Borel (1998), Subduction and obduction processes in the Swiss Alps, *Tectonophysics*, *296*, 159–204, doi:10.1016/S0040-1951(98)00142-5.

Stephenson, J., K. Gallagher, and C. C. Holmes (2006), A Bayesian approach to calibrating apatite fission track annealing models for laboratory and geological timescales, *Geochim. Cosmochim. Acta*, *70*, 5183–5200, doi:10.1016/j.gca.2006.07.027.

Stüwe, K., L. White, and R. Brown (1994), The influence of eroding topography on steady-state isotherms. Application to fission track analysis, *Earth Planet. Sci. Lett.*, *124*, 63–74, doi:10.1016/0012-821X(94)00068-9.

Vernon, A. J., P. A. van der Beek, H. D. Sinclair, and M. K. Rahn (2008), Increase in late Neogene denudation of the European Alps confirmed by analysis of a fission-track thermochronology database, *Earth Planet. Sci. Lett.*, *270*, 316–329, doi:10.1016/j.epsl.2008.03.053.

von Raumer, J., J. Abrecht, F. Bussy, B. Lombardo, R. P. Menot, and U. Schaltegger (1999), The Palaeozoic metamorphic evolution of the Alpine External Massifs, *Schweiz. Mineral. Petrogr. Mitt.*, *79*, 5–22.

Wagner, G. A., and G. M. Reimer (1972), Fission track tectonics: The tectonic interpretation of fission track apatite ages, *Earth Planet. Sci. Lett.*, *14*, 263–268, doi:10.1016/0012-821X(72)90018-0.

Willett, S. D., F. Schlunegger, and V. Picotti (2006), Messinian climate change and erosional destruction of the central European Alps, *Geology*, *34*, 613–616, doi:10.1130/G22280.1.

Williamson, J. H. (1968), Least squares fitting of a straight line, *Can. J. Phys.*, *46*, 1845–1847.

Zhang, P., P. Molnar, and W. R. Downes (2001), Increased sedimentation rates and grain sizes 2–4 Myr ago due to the influence of climate change on erosion rates, *Nature*, *410*, 891–897, doi:10.1038/35073504.

J. Foeken and F. M. Stuart, Isotope Geosciences Unit, Scottish Universities Environmental Research Centre, De Boelelaan 1085-1087, East Kilbride G75 0QF, UK.

C. Persano, Department of Geographical and Earth Sciences, University of Glasgow, University Avenue, Glasgow G12 8QQ, UK.

H. D. Sinclair, School of Geosciences, University of Edinburgh, Geography Building, Drummond Street, Edinburgh EH9 3JW, UK.

P. A. van der Beek, Laboratoire de Géodynamique des Chaînes Alpines, Université Joseph Fourier, BP 53, F-38041 Grenoble CEDEX, France.

A. J. Vernon, Department of Geosciences, University of Arizona, 1040 E 4th Street, Tucson, AZ 85721, USA. (ajvernon@email.arizona.edu)